



Three-dimensional thermomechanical modeling of oceanic spreading initiation and evolution

Taras V. Gerya

Institute of Geophysics, ETH Zürich, Sonneggstrasse 5, 8092 Zürich, Switzerland

ARTICLE INFO

Article history:

Received 8 May 2012

Received in revised form 2 October 2012

Accepted 18 October 2012

Available online 29 October 2012

Edited by Mark Jellinek

Keywords:

Mid-ocean ridge

Transform fault

Rifting

Oceanic crust growth

ABSTRACT

This work employs high-resolution 3D thermomechanical numerical models of the incipient oceanic spreading to investigate nucleation and long-term evolution of ridge-transform spreading patterns. The Eulerian–Lagrangian visco-plastic model allows for large strains and accounts for plate cooling by both heat conduction and hydrothermal circulation as well as for partial melting of the asthenosphere and oceanic crust growth by magmatic accretion. According to the numerical experiments, the oceanic spreading pattern depends strongly on the initial offset of spreading centers and the magnitude of fracture healing rate. Three different characteristic long-term spreading modes are obtained: (1) ridge-transform patterns, (2) single ridges and (3) spreading centers with an intermediate plate. Ridge-transform oceanic spreading patterns form gradually from moderate initial offsets of 40–60 km and become fully established several million years after the plate breakup. Moreover, it is demonstrated on the basis of simple analyses that the ridge-transform system is a long-term plate growth pattern that is generally different from an initial plate rifting pattern. Geometry of the ridge-transform system is governed by geometrical requirements (180° rotational symmetry for open space occupation) for simultaneous accretion and displacement of new plate material within two offset spreading centers connected by a sustaining rheologically weak transform fault. According to these requirements, the characteristic spreading-parallel orientation of oceanic transform faults is the only thermomechanically consistent steady state orientation. Results of numerical experiments compare well with both incipient and mature ridge-transform systems observed in nature.

© 2012 Elsevier B.V. All rights reserved.

1. Introduction

The characteristic pattern of mid-ocean ridges, sectioned by transform faults stands as an inherent feature of terrestrial plate tectonics. A fundamental unresolved problem is how this pattern formed and why it is maintained. One common view is that oceanic transform faults are typically inherited from the continental plate breakup (e.g., Wilson, 1965; Lister et al., 1986; Cochran and Martinez, 1988; McClay and Khalil, 1998). This view is, in particular, based on a geometric correspondence between passive margins and mid-ocean ridges, which is especially prominent for the South Atlantic Ridge and the West African coast. Several lines of evidence support this view by showing that stepping half-grabens (Cochran and Martinez, 1988; McClay and Khalil, 1998), segmented gravity and magnetic anomalies (Behn and Lin, 2000), or segmented weak regions (Watts and Stewart, 1998) along passive margins lead to the formation of transform faults. Indeed, Lister et al. (1986) proposed that passive margins are characterized by an orthogonal set of normal and transfer faults; the latter potentially developing into transform faults. In contrast, a number of other observations

suggest that the characteristic orthogonal ridge – transform fault pattern is not directly inherited from the earlier rift geometry and a one-to-one correspondence between the transfer faults in the continental rift stage and transform faults in the oceanic spreading stage does not exist (Bosworth, 1986; Taylor et al., 1995, 2009). Bosworth (1986) and Rosendahl (1987), amongst others, proposed that half grabens, delimited along strike by accommodation zones, are the fundamental units of rift architecture. Accommodation zones are generally oblique features (Bosworth, 1986; Jarrige et al., 1990), making them unlikely precursors of transform faults (Bosworth, 1986). In addition, high-resolution bathymetry data from the incipient oceanic spreading regions, such as Woodlark Basin, Gulf of Aden and NW Australia, show that spreading segments nucleate en echelon in overlapping rift basins and that initial spreading offsets, where present, are often non-transform (Taylor et al., 1995, 2009). Thus, an ambiguity remains on how the transform faults originated and when, how and why did the orthogonal ridge-transform fault pattern form.

Due to the limited availability of data, detailed interpretations of nucleation and evolution of ridge-transform oceanic spreading patterns are difficult and controversial (Lister et al., 1986; Bosworth, 1986; Dauteuil and Brun, 1996; Taylor et al., 1995, 2009),

E-mail address: taras.gerya@erdw.ethz.ch

thus analogue and numerical models have been employed (see recent review by Gerya, 2012 and references therein). Two main styles of analogue models have been examined: (i) thermomechanical freezing wax models with accreting and cooling plates (Oldenburg and Brune, 1972; O'Bryan et al., 1975; Ragnarsson et al., 1996; Katz et al., 2005) and (ii) mechanical models with viscous mantle and brittle lithosphere (Dauteuil and Brun, 1993; Dauteuil et al., 2002; Marques et al., 2007; Tentler and Acocella, 2010). The freezing wax models reproduced characteristic orthogonal ridge – transform fault patterns but often produced open spreading centers with exposed liquid wax, which is dissimilar to nature. On the other hand, in the mechanical models, new lithosphere is not accreted in spreading centers, which is incompatible with oceanic spreading. Also, the rheological properties of the materials used in thermomechanical and mechanical analogue models are highly simplified compared to the temperature-, pressure- and stress-dependent visco-elasto-plastic rheology of multi-phase oceanic lithosphere (e.g., Ranalli, 1995; Buck et al., 2005) subjected to spontaneous weakening and shear-localization in a wide range of P-T conditions (e.g., Bercovici and Ricard, 2012).

Numerical models of transform fault nucleation (Hieronymus, 2004; Choi et al., 2008) and continental rifting (Allken et al., 2011, 2012) mostly focused on spontaneous plate fragmentation (rifting) processes and demonstrated that orthogonal and oblique ridge-transform linkage patterns can spontaneously arise from small, initially offset perturbations (weak seeds) in the plate structure. It was shown numerically with 2D mechanical models (Hieronymus, 2004) that in this case only five fundamental spreading modes can form: orthogonal transform faults, microplates, overlapping spreading centers, zigzag ridges and oblique connecting spreading centers. It was also demonstrated using 3D visco-elasto-plastic thermomechanical models (Choi et al., 2008) that under condition of variable ratio of thermal stress to spreading-induced stress, the orthogonal pattern marks transition from the overlapping to the connecting mode. Based on 3D visco-plastic mechanical models employing a plastic rheology with strain softening, Allken et al. (2011, 2012) indicated that rift offset and viscosity of the lower crust are the main controls on the efficiency of rift propagation and the style of rift segment interaction during continental rifting. Indeed, strain reached in previous numerical experiments was too small to test the evolution of ridge-transform patterns during long-term spreading associated with significant plate accretion. Recent large-strain numerical experiments (Gerya, 2010a) focused on spontaneous nucleation of transform faults at a single straight ridge but the initiation and long-term evolution of ridge-transform oceanic spreading patterns after plate breakup remained unaddressed.

In the present paper we build on the results of previous numerical experiments to develop 3D thermomechanical numerical model of long-term oceanic spreading starting from the culminating stages of continental rifting. The principal goal of this study is to model the dynamics of an incipient spreading process and understand when, how and why typical ridge-transform spreading patterns can be established during the history of oceanic spreading.

2. Numerical model

This work employs high-resolution 3D thermomechanical numerical models of the incipient oceanic spreading to investigate nucleation and evolution of ridge-transform oceanic spreading patterns. The Eulerian–Lagrangian visco-plastic model with an internal free surface (Fig. 1) allows for large strains and spontaneous oceanic crust growth by magmatic accretion. The employed numerical technique (Gerya, 2010a,b) is based on a combination of a finite difference method applied on a uniformly spaced staggered finite difference grid, with the marker-in-cell technique.

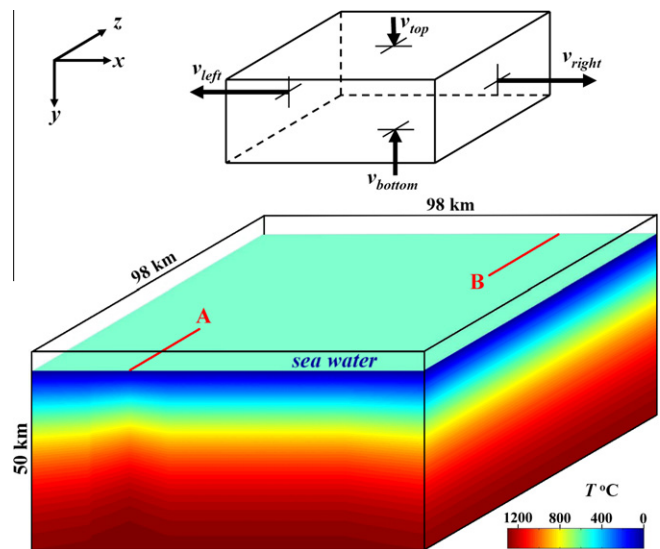


Fig. 1. Initial model setup and boundary conditions for 3D thermomechanical numerical experiments. Boundary conditions are constant spreading rate in x -direction ($v_{\text{spreading}} = v_{\text{left}} + v_{\text{right}}$, where $v_{\text{left}} = v_{\text{right}}$) and compensating vertical inflow velocities through the upper and lower boundaries (v_{top} and v_{bottom}) are chosen to ensure conservation of volume of the model domain and constant average 5 km thickness of the sea water layer $[(v_{\text{top}} + v_{\text{bottom}})/50 = (v_{\text{left}} + v_{\text{right}})/98]$, where $v_{\text{top}}/5 = v_{\text{bottom}}/45$; front and back boundaries in the x - y plane are free slip. A water-loaded free surface condition for the upper plate boundary is implemented by using a weak layer approach (e.g., Schmeling et al., 2008; Gerya, 2010b; Cramer et al., 2012): the weak 5 km thick sea water layer has a characteristic density of 1000 kg/m³ and a viscosity of 10¹⁸ Pa s to ensure small stresses (<10⁵ Pa) along the upper plate interface. The symmetric initial thermal structure is perturbed in two places where offset linear thermal anomalies (weak seeds) A and B are prescribed by gently elevated geotherm. Thermal boundary conditions are insulating (zero heat flux) on all boundaries with except of the upper and lower boundaries, over which a constant temperature of 273 and 1600 K is prescribed, respectively.

2.1. Model setup

The initial model setup corresponds to the onset of oceanic spreading along an already thinned, idealized rifted margin with a 7–20 km thick crust (Table 1). Similarly to previous numerical models of spontaneous plate fragmentation (e.g., Hieronymus, 2004; Choi et al., 2008; Allken et al., 2011, 2012), two linear thermal perturbations (weak seeds) with an offset of 30–60 km are imposed at the bottom of the lithospheric mantle (Fig. 1). Prescribing of offset perturbations (weak seeds) is a standard approach for both analogue and numerical models of rifting and spreading (e.g., Hieronymus, 2004; Choi et al., 2008; Tentler and Acocella, 2010; Allken et al., 2011, 2012). This approach is consistent with observations on incipient oceanic spreading regions where spreading segments nucleate en echelon in overlapping rift basins with non-transform spreading offsets (Taylor et al., 1995, 2009). The magnitude of the offsets varies in nature and is often in the range of several tens of kilometers (e.g., Bosworth, 1986; Taylor et al., 1995, 2009). In our model the initially offset thermal perturbations affect (but not strictly define) positions of the individual spreading centers. It should also be mentioned that both linear and point-like weak seeds trigger nucleation of elongated rift structures which are nearly orthogonal to the extension direction (e.g., Hieronymus, 2004; Choi et al., 2008; Tentler and Acocella, 2010; Allken et al., 2011, 2012). The modeled (full) spreading rates ($v_{\text{spreading}}$) range from 3.8 to 5.7 cm/yr, which simulates incipient slow- to intermediate-spreading ridge (Taylor et al., 2009). The Eulerian computational domain is equivalent to 98 × 98 × 50 km (Fig. 1) and is resolved with a regular rectangular grid of 197 × 197 × 101 nodes and contains 34 million randomly distributed Lagrangian markers. Larger 202 × 98 × 50 km models with 405 × 197 × 101 nodes and

Table 1
Conditions and results of numerical experiments.

Model	Width (km)	Crust thickness (km)	Spreading rate (cm/yr)	Nu	C_0/C_1 (MPa)	$\dot{\epsilon}_{\text{heating}}$ (1/s)	Max. viscosity (Pa s)	Molten rock viscosity (Pa s)	Depth of 1000 °C isotherm (km)	Initial offset (km)	Initial rifting pattern (0–2 Myr)	Young spreading pattern (2–5 Myr)	Mature spreading pattern (>5 Myr)
dard	98	7	3.8	2	10/3	0	10^{24}	10^{18}	20	60	OSC ^a with bending middle plate, OSC linked by oblique fault	Two parallel ridges with fragmented middle plate	Two parallel ridges with growing middle plate divided by TF
dare	98	7	3.8	2	10/3	0	10^{22}	10^{18}	20	60	OSC with RMP	RMP accretion with PTF development	ORTP, fragmented plates
darf	98	7	3.8	2	10/3	0	10^{22}	10^{18}	12	60	OSC with RMP	OSC with growing RMP, RMP accretion	ORTP, fragmented plates
darj	98	7	3.8	2	10/3	0	10^{22}	10^{18}	12	20	SCs facing each other	Single ridge with RMP	Accretion of RMP, single straight ridge
dark	98	7	3.8	2	10/3	0	10^{22}	10^{18}	12	40	SCs linked by oblique fault, two RMPs	Accretion of RMPs, single curved ridge	Single curved ridge with an oblique middle section
darl	98	7	3.8	2	10/3	0	10^{22}	10^{18}	20	20	SCs facing each other, two RMPs	Accretion of RMPs, single ridge	No results
darm	98	7	3.8	2	10/3	0	10^{22}	10^{18}	20	40	SCs linked by oblique fault, two RMPs	Accretion of RMPs, transient TF	ZOT, single straight ridge
darn	98	7	3.8	2	10/3	0	10^{24}	10^{18}	20	20	SCs facing each other	No results	No results
darp	98	7	3.8	2	10/3	0	10^{22}	10^{18}	13	40	SCs linked by oblique fault, RMP	RMP accretion with PTF development	ORTP
darq	98	7	3.8	2	10/3	0	10^{22}	10^{18}	13	50	SCs linked by orthogonal PTF, two RMPs	ORTP	ORTP
darr	98	7	3.8	2	10/3	0	10^{22}	10^{18}	13	60	OSC with RMP, orthogonal PTF cutting RMP	ORTP	ORTP
dars	98	7	3.8	2	10/3	10^{-13}	10^{22}	10^{18}	13	40	SCs linked by oblique PTF	Transient IRTP, ZOT	Single straight ridge
dart	98	7	3.8	2	10/3	10^{-13}	10^{22}	10^{18}	13	50	SCs linked by oblique PTF	ORTP	ORTP
daru	98	7	3.8	2	10/3	10^{-13}	10^{22}	10^{18}	13	60	OSC with RMP	RMP accretion with two PTFs development	ORTP with two TF and an intermediate SC
darv	202	7	3.8	2	10/3	10^{-13}	10^{22}	10^{18}	13	60	OSC with RMP	OSC with growing RMP	OSC with growing RMP, two parallel ridges with growing middle plate
darw	202	15	3.8	2	10/3	10^{-13}	10^{22}	10^{18}	21	60	OSC with RMP	OSC with growing RMP	OSC with growing RMP, two parallel ridges with growing middle plate
darx	98	7	3.8	2	10/3	3×10^{-13}	10^{22}	10^{18}	13	50	SCs linked by oblique PTF	IRTTP	IRTTP
dary	98	7	3.8	2	20/3	10^{-13}	10^{22}	10^{18}	13	50	SCs linked by oblique PTF	ORTP	ORTP
darz	98	15	3.8	2	10/3	10^{-13}	10^{22}	10^{18}	21	50	SCs linked by oblique PTF	IRTTP	Transient IRTTP, ZOT, single straight ridge
dasa	98	7	3.8	2	10/3	10^{-12}	10^{22}	10^{18}	13	50	SCs linked by oblique PTF	Curved single ridge with an oblique middle section	No results
dasb	98	7	3.8	2	10/3	3×10^{-13}	10^{23}	10^{18}	13	50	SCs linked by oblique PTF	IRTTP	IRTTP
dasc	98	7	3.8	2	10/3	3×10^{-13}	10^{24}	10^{18}	13	50	SCs linked by oblique PTF	IRTTP	IRTTP
dasd	98	15	3.8	2	10/3	3×10^{-13}	10^{22}	10^{18}	21	50	SCs linked by oblique PTF	Two TF with an intermediate SC, disappearance of one TF via ZOT	IRTTP with one TF
dase	98	12	3.8	2	10/3	3×10^{-13}	10^{22}	10^{18}	21	50	SCs linked by oblique PTF	IRTTP	IRTTP

(continued on next page)

Table 1 (continued)

Model	Width (km)	Crust thickness (km)	Spreading rate (cm/yr)	Nu	C_0/C_1 (MPa)	$\dot{\epsilon}_{\text{healing}}$ (1/s)	Max. viscosity (Pa s)	Molten rock viscosity (Pa s)	Depth of 1000 °C isotherm (km)	Initial offset (km)	Initial rifting pattern (0–2 Myr)	Young spreading pattern (2–5 Myr)	Mature spreading pattern (>5 Myr)
dasf	98	9	3.8	2	10/3	3×10^{-13}	10^{22}	10^{18}	21	50	SCs linked by oblique PTF	IRTP	IRTP
dasg	98	12	3.8	2	10/3	3×10^{-13}	10^{22}	10^{18}	29	50	OSC with bending plate in between, OSC with RMP	OSC with growing RMP	OSC with growing RMP, two parallel ridges with growing middle plate
dash	98	15	5.7	2	10/3	3×10^{-13}	10^{22}	10^{18}	21	50	SCs linked by oblique PTF, two TF with an intermediate SC	Transient IRTP with two TF and an intermediate SC	Disappearance of two TFs via ZOTs, single curved ridge with an oblique middle section
dasi	98	15	5.7	4	10/3	3×10^{-13}	10^{22}	10^{18}	21	50	SCs linked by oblique PTF, IRTP	Transient IRTP, disappearance of one TF via ZOT	Single straight ridge
dasj	98	15	3.8	2	10/5	3×10^{-13}	10^{22}	10^{18}	21	50	SCs linked by oblique PTF	Transient IRTP with two TFs and an intermediate SC, disappearance of two TFs via ZOTs	Single curved ridge with an oblique middle section
dask	98	15	3.8	2	10/3	3×10^{-13}	10^{22}	10^{19}	21	50	SCs linked by oblique PTF	Transient IRTP	Disappearance of TF via ZOT, curved single ridge with an oblique middle section
dasl ^b	98	15	3.8	2	10/3	3×10^{-13}	10^{22}	10^{18}	21	50	SCs linked by oblique PTF	Transient IRTP	Disappearance of TF via ZOT, single curved ridge with an oblique middle section
dasm	98	15	3.8	2	15/3	10^{-13}	10^{24}	10^{18}	21	50	SCs linked by oblique PTF	ORTP	ORTP, appearance of growing RMP inside TF
dasn	98	15	3.8	2	15/3	10^{-13}	10^{24}	10^{18}	29	50	OSC with bending plate in between	Two parallel ridges with growing middle plate	Two parallel ridges with growing middle plate
daso	202	7	3.8	2	10/3	10^{-13}	10^{24}	10^{18}	13	40	SCs linked by oblique PTF	ORTP	ORTP, disappearance of TF via ZOT, single straight ridge
dasr	202	20	3.8	2	10/3	10^{-13}	10^{24}	10^{18}	21	40	SCs linked by oblique PTF	ORTP	ORTP
dasx	202	20	3.8	2	20/3	10^{-13}	10^{24}	10^{18}	21	40	SCs linked by oblique PTF	ORTP	ORTP
dasy ^b	98	7	3.8	2	20/3	10^{-13}	10^{22}	10^{18}	13	50	OSC with bending plate in between, OSC with RMP	Fragmentation of RMP by orthogonal PTF, ORTP with asymmetric accretion	Disappearance of TF, single curved ridge with asymmetric accretion
dasz ^b	98	7	3.8	2	10/3	10^{-13}	10^{22}	10^{18}	13	50	OSC with RMP, RMP accretion with PTF development	ORTP	ORTP

^a Abbreviations: SC = spreading center, OSC = overlapping spreading centers (Fig. 9c), PTF = proto-transform fault (Fig. 3b), TF = transform fault (spreading-parallel, Fig. 3e), RMP = rotating microplate (Figs. 5a, 9d and e), ORTP = orthogonal ridge-transform pattern (Fig. 3e), IRTP = inclined ridge-transform pattern (Fig. 6f), ZOT = zero offset transform (zero offset fracture zone, Fig. 8c).

^b Dry olivine flow law (Ranalli, 1995) with $\sigma_{\text{yield}} = 3$ MPa is used for the partially molten mantle.

68 million markers were also used in a limited number of experiments (Table 1).

The momentum, mass and heat conservation equations are solved with the thermomechanical code I3ELVIS (Gerya and Yuen, 2007) on the non-deforming Eulerian grid whereas the advection of transport properties including viscosity, plastic strain, temperature etc. is performed by advecting the Lagrangian markers. Lagrangian markers leave the Eulerian model domain through the left and right lateral boundaries. Material enters through the top and the bottom of the model as sea water and mantle markers, respectively. This Eulerian–Lagrangian numerical modeling scheme with open boundaries allows for an infinitely long plate separation with the use of a laterally limited Eulerian computational domain. The initial thermal structure and lithospheric thickness is defined by varying the depth of 1000 °C isotherm according to the cooling profile of a semi-infinite, half-space (Turcotte and Schubert, 2002).

2.2. Modeling of mid-ocean ridge processes

Fig. 2 shows a conceptual model of oceanic spreading implemented in the present study. In some aspects, this model is more complex than previous 3D numerical modeling approaches (Choi et al., 2008; Allken et al., 2011, 2012; Gerya, 2010a). This is mainly dictated by the necessity to address a relatively complex and long-lasting transition between the plate breakup and oceanic spreading (e.g., Taylor et al., 1995, 2009). Thus, long-term crustal and lithospheric deformation, accretion and cooling processes have to be captured (e.g., Buck et al., 2005; Olive et al., 2010; Theissen-Krah et al., 2011) thereby allowing for direct testing of our numerical results with crustal faulting, growth and topography patterns observed in natural incipient oceanic spreading regions (e.g., Taylor et al., 1995, 2009). Therefore, the conceptual model accounts for the following key processes which were suggested to be critical for realistic modeling of plate breakup and oceanic spreading (e.g., Buck et al., 2005; Gregg et al., 2009; Katz, 2010; Olive et al., 2010; Theissen-Krah et al., 2011; Montesi et al., 2011): (i) thermal accretion of the oceanic mantle lithosphere resulting in the plate thickness growth, (ii) partial melting of the asthenospheric mantle, melt extraction and percolation toward the ridge resulting in crustal growth, (iii) magmatic accretion of the new oceanic crust under the ridge and (iv) hydrothermal circulation at the axis of the ridge, resulting in excess cooling of the crust. These physical processes are included in our numerical model in a simplified manner. Below we explain how each process was introduced.

Thermal accretion of the mantle lithosphere is modeled by solving the heat conduction equation combined with a temperature-dependent viscosity for the non-molten mantle (dry olivine flow law, Ranalli, 1995). Consequently, cooling asthenospheric mantle become rheologically strong and accretes spontaneously to the bottom of the oceanic lithosphere.

Hydrothermal circulation at the axis of the ridge producing rapid cooling of the new oceanic crust (e.g., Theissen-Krah et al., 2011) is

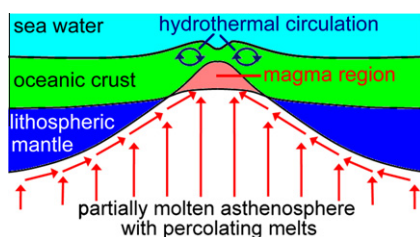


Fig. 2. Conceptual model of oceanic spreading implemented in this study. See text for more details.

parameterized with an enhanced thermal conductivity of the crust based on the following equation (Gregg et al., 2009)

$$K_{\text{eff}} = k + k_0(Nu - 1) \times \exp[A(2 - T/T_{\text{max}} - y/y_{\text{max}})] \quad (1)$$

where T is the temperature (°C) k is the thermal conductivity of dry rocks (W/m/K) [$k = 0.73 + 1293/(T + 77)$ for the mantle and $k = 1.18 + 474/(T + 77)$ for the crust (Clauser and Huenges, 1995)], $k_0 = 3$ W/m/K is the reference thermal conductivity, $Nu = 2-4$ is the assumed Nusselt number for the hydrothermal circulation (Gregg et al., 2009), $A = 0.75$ is a smoothing factor, T_{max} is the cutoff maximum temperature (600 °C), y is depth (km), and $y_{\text{max}} = 6$ km is the cutoff maximum depth of hydrothermal circulation. Also, in order to insure an efficient heat transfer from the upper surface of the plate in the Eulerian model, thermal conductivity of the sea water layer above this plate (Fig. 1) is taken to be hundred times higher (200 W/m/K) than that of the dry mantle (1–4 W/m/K).

Partial melting of the asthenospheric mantle, melt extraction and percolation toward the ridge is implemented in a highly simplified manner. According to our model, crustal growth at the ridge is balanced by the melt production and extraction in the mantle. However, melt percolation toward the ridge (e.g., Katz, 2010) is not modeled directly and considered to be nearly instantaneous (Connolly et al., 2009). The standard (i.e. without melt extraction) volumetric degree of mantle melting M_0 changes with pressure and temperature according to the parameterized batch melting model of Katz et al. (2003). Lagrangian markers track the amount of melt extracted during the evolution of each experiment. The total amount of melt, M , for every marker takes into account the amount of previously extracted melt and is calculated as (Nikolaeva et al., 2008)

$$M = M_0 - \sum_n \cdot M_{\text{ext}} \quad (2)$$

where $\sum_n \cdot M_{\text{ext}}$ is the total melt fraction extracted during the previous n extraction episodes. The rock is considered non-molten (refractory) when the extracted melt fraction is larger than the standard one (i.e. when $\sum_n \cdot M_{\text{ext}} > M_0$). If $M > 0$ for a given marker, the melt fraction $M_{\text{ext}} = M$ is extracted and $\sum_n \cdot M_{\text{ext}}$ is updated. The extracted melt fraction M_{ext} is assumed to propagate much faster than the plates deform (Connolly et al., 2009). Hence, the instantaneous transmission of extracted melt to the magma chamber is reasonable. Similarly to Gregg et al. (2009), a wide pooling region for the melt extraction and migration is assumed and melts produced in the entire model are added to the shallowest regions where mantle melting conditions are still achieved. Such regions are typically located beneath the ridge axis and inside intra-transform spreading centers where wedge-shaped magma regions (Fig. 2) spontaneously form by accumulation of the introduced melts. In order to ensure melt volume conservation and account for mantle compaction and subsidence in response to the melt extraction, melt addition to the bottom of the magma region is performed at every time step by converting shallowest markers of hot partially molten mantle into magma markers. The total volume of these magma markers matches the total volume of extracted melt computed for the time step.

Magmatic accretion of the new oceanic crust is modeled by spontaneous cooling and crystallization of melts at the walls of the lower-crustal magma regions (e.g., Wanless and Shaw, 2012). This simple crust accretion algorithm does not account for volcanic and plutonic (e.g., dyking, Buck et al., 2005; Wanless and Shaw, 2012) processes above the magma regions, neither does it account for internal convection, melt segregation and crystal differentiation inside these regions (e.g., Wanless and Shaw, 2012). The effective density of the molten crust in the magma region is calculated as

$$\rho_{\text{eff}} = \rho_{\text{solid}} \left(1 - M + M \frac{\rho_{\text{omolten}}}{\rho_{\text{solid}}} \right) \div, \quad (3)$$

where local melt fraction M is computed from the simple linear batch melting model (Gerya, 2010b)

$$M = 0 \quad \text{when} \quad T < T_{\text{solidus}}, \quad (4a)$$

$$M = \frac{(T - T_{\text{solidus}})/(T_{\text{liquidus}} - T_{\text{solidus}})}{T_{\text{solidus}} < T < T_{\text{liquidus}}} \quad \text{when} \quad (4b)$$

$$M = 1 \quad \text{when} \quad T > T_{\text{liquidus}}, \quad (4c)$$

where $T_{\text{solidus}} = 1327 + 0.091P$ and $T_{\text{liquidus}} = 1423 + 0.105P$ are, respectively, solidus and liquidus temperature (K) of the crust (Hess, 1989) at a given pressure P (MPa). $\rho_{\text{solid}} = 3000 \text{ kg/m}^3$ and $\rho_{\text{molten}} = 2800 \text{ kg/m}^3$ are the standard densities of solid and molten crust, respectively and ρ_{solid} is the density of solid crust at given P and T computed from

$$\rho_{\text{solid}} = \rho_{\text{solid}} \times [1 - \alpha(T - 298)] \times [1 + \beta(P - 0.1)], \quad (5)$$

where $\alpha = 3 \times 10^{-5} \text{ 1/K}$ and $\beta = 10^{-5} \text{ 1/MPa}$ are thermal expansion and compressibility of the crust. The effect of latent heating due to equilibrium crystallization of the crust from the magma regions is included implicitly by increasing the effective heat capacity ($C_{p\text{eff}}$) and the thermal expansion (α_{eff}) of the partially crystallized/molten rocks ($0 < M < 1$), calculated as (Gerya, 2010b):

$$C_{p\text{eff}} = C_p + Q_L \left(\frac{M}{T} \right)_{P=\text{const}}, \quad (6)$$

$$\alpha_{\text{eff}} = \alpha + \rho \frac{Q_L}{T} \left(\frac{M}{P} \right)_{T=\text{const}}, \quad (7)$$

where $C_p = 1000 \text{ J/kg}$ is the heat capacity of the solid crust and $Q_L = 380 \text{ kJ/kg}$ is the latent heat of crystallization of the crust (Turcotte and Schubert, 2002). The employed linear crustal crystallization algorithm is simplified and neglects the non-linearity of the melt fraction decrease with decreasing temperature between T_{liquidus} and T_{solidus} . However, this simplification should mainly affect melt crystallization dynamics inside relatively small lower-crustal magma region (Fig. 2) without having dominant effects on the rheological and density structure of the entire model.

2.3. Rheological model

The rheological model assumes a constant low viscosity (10^{18} – 10^{19} Pa s) for the partially molten crustal and mantle rocks, and a visco-plastic rheology for the lithospheric plates, with a realistic temperature and strain rate dependent viscosity computed according to experimentally determined flow laws (Ranalli, 1995). We use the dry olivine flow law for the mantle and the plagioclase (An_{75}) flow law for the crust. An upper viscosity cutoff limit of 10^{22} – 10^{24} Pa s was also applied for the lithospheric viscosity (Table 1). Compared to previous models of mid-ocean ridges (Hieronymus, 2004; Buck et al., 2005; Choi et al., 2008), this rheological model does not account for elasticity of the lithosphere and neglects thermally induced stresses. Standard brittle/plastic rheology of solid rocks assumes fracture-related strain weakening (Lavie et al., 2000; Huismans and Beaumont, 2002; Hieronymus, 2004; Choi et al., 2008; Gerya, 2010a; Allken et al., 2011, 2012), and is implemented by using a plate strength limitation of the form

$$\sigma_{II} \leq C_\gamma + \phi_\gamma (P - P_f) \quad (8)$$

$$\phi_\gamma = 1 \quad \text{when} \quad P < P_f \quad (\text{tensile fracture})$$

$$\phi_\gamma = 0.6(1 - \gamma/\gamma_0) \quad \text{for} \quad \gamma \leq \gamma_0 \quad \text{and} \quad \phi_\gamma = 0 \quad \text{for} \quad \gamma > \gamma_0 \\ \text{when} \quad P \geq P_f \quad (\text{confined fracture}) \quad (9)$$

$$C_\gamma = C_0 + (C_1 - C_0)\gamma/\gamma_0 \quad \text{for} \quad \gamma \leq \gamma_0 \quad \text{and} \quad C_\gamma = C_1 \quad \text{for} \quad \gamma > \gamma_0$$

$$P_f = \rho_f g y, \quad (11)$$

$$\gamma = \int \sqrt{\frac{1}{2} (\dot{\epsilon}_{ij(\text{plastic})})^2} dt - \int \dot{\epsilon}_{\text{healing}} dt, \quad (12)$$

$$\sigma_{II} = \sqrt{\frac{1}{2} (\sigma'_{ij})^2}, \quad (13)$$

where σ_{II} is second stress invariant (Pa), P is dynamic pressure on solids (Pa), P_f is fluid pressure (Pa), y is vertical coordinate (m), $g = 9.81 \text{ m/s}^2$ is gravitational acceleration, $\rho_f = 1000 \text{ kg/m}^3$ is water density, $\gamma \geq 0$ is integrated plastic strain ($\gamma_0 = 1$ is the upper strain limit for the fracture-related weakening), t is time (s), $\dot{\epsilon}_{ij(\text{plastic})}$ is plastic strain rate tensor, $\dot{\epsilon}_{\text{healing}}$ is fracture healing rate, C_γ is the rock strength at $P - P_f = 0$ (for both confined and tensile fracture) which depends on the plastic strain γ and C_0 and C_1 are the initial and final strength values for the fracture-related weakening, respectively. The stress limitation for tensile fracture is formulated from a theoretical criterion (Rozhko et al., 2007) for tensile failure of a fluid-filled crack. This criterion is based on Griffith's theory (Murrell, 1964) and has been verified experimentally (Jaeger, 1963). Strain weakening assumed in the model is similar to those in previous numerical studies of mid-ocean ridges (Hieronymus, 2004; Choi et al., 2008; Gerya, 2010a) and continental rifting (Huismans and Beaumont, 2002; Allken et al., 2011). It is related, in particular, to water and melt percolation and textural modifications along fault zones and their intense serpentinization that strongly decreases the strength of fractured fault rocks (Huismans and Beaumont, 2002; Escartín et al., 2001; Hilairat et al., 2007; Bercovici and Ricard, 2012). Partial healing of deactivated, slowly creeping fractures (e.g., Lyakhovskiy and Ben-Zion, 2008) was applied in the majority of experiments by using an imposed constant healing rate $\dot{\epsilon}_{\text{healing}}$ (Table 1) which reduces the accumulated plastic strain γ with time. When the second invariant of local strain plastic strain rate tensor $\sqrt{\frac{1}{2} (\dot{\epsilon}_{ij(\text{plastic})})^2}$ inside a fault is greater than $\dot{\epsilon}_{\text{healing}}$, the accumulated strain γ increases with time according to Eq. (12) and brittle-plastic strength decreases according to Eqs. (9), (10). In contrast, when the second invariant becomes smaller than $\dot{\epsilon}_{\text{healing}}$, the accumulated strain γ start to decrease (Eq. 12) and brittle-plastic strength recovery of the fault occurs (Eqs. (9), (10)). This simple brittle/plastic weakening/healing model, in which γ serves as a damage/recovery measure, implies that the magnitude of healing rate $\dot{\epsilon}_{\text{healing}}$ should be comparable with the magnitude of strain rate $\dot{\epsilon}_{ij(\text{plastic})}$ inside active faults. Given that spontaneously forming brittle/plastic faults are localized within one to two grid cells (e.g., Buitter et al., 2006), both strain weakening limit γ_0 and healing rate $\dot{\epsilon}_{\text{healing}}$ should linearly scale with the grid step (e.g., Lavie et al., 2000). This scaling makes the weakening and healing to be dependent on the absolute amount of material displacement along the walls of spontaneously forming faults, irrespective of the numerical resolution (e.g., Lavie et al., 2000). In particular, the adopted $\gamma_0 = 1$ value implies 1000 m of relative displacement ($d = 2\gamma_0 \Delta x$, where $\Delta x = 500 \text{ m}$ is the model grid step) between the walls of a fault. Similarly, the adopted $\dot{\epsilon}_{\text{healing}} = 10^{-13} \text{ s}^{-1}$ (Table 1) implies brittle/plastic strength recovery for displacement rates less than 3 mm/yr (10^{-10} m/s , $2 \dot{\epsilon}_{\text{healing}} \Delta x$) between the walls of a fault. It should be pointed out that the employed simple strain weakening/healing model (Lavie et al., 2000; Huismans and Beaumont, 2002; Hieronymus, 2004; Choi et al., 2008; Lyakhovskiy and Ben-Zion, 2008; Gerya, 2010a; Allken et al., 2011, 2012) is purely phenomenological and does not directly reflect the physics involved in various weakening/healing processes. These processes may in particular involve fluid and melt percolation, grain damage and growth, structural annealing and Zener pinning in multi-phase polycrystalline lithospheric rocks

(e.g., Bercovici and Ricard, 2012). Therefore, further theoretical development (e.g., Bercovici and Ricard, 2012) and numerical implementation of more sophisticated and realistic lithospheric weakening/healing models is required in the future.

3. Numerical results

Table 1 summarizes conditions and results of 38 numerical experiments conducted during this study. In these experiments we varied most of the model parameters and results of representa-

tive models are described below. Ridge-transform spreading patterns as well as other characteristic young and mature oceanic spreading modes are systematically documented based on these numerical experiments.

3.1. Reference model development

Fig. 3 represents typical evolution of the numerical model associated with the spontaneous development of offset oceanic spreading centers evolving into the typical orthogonal ridge – transform

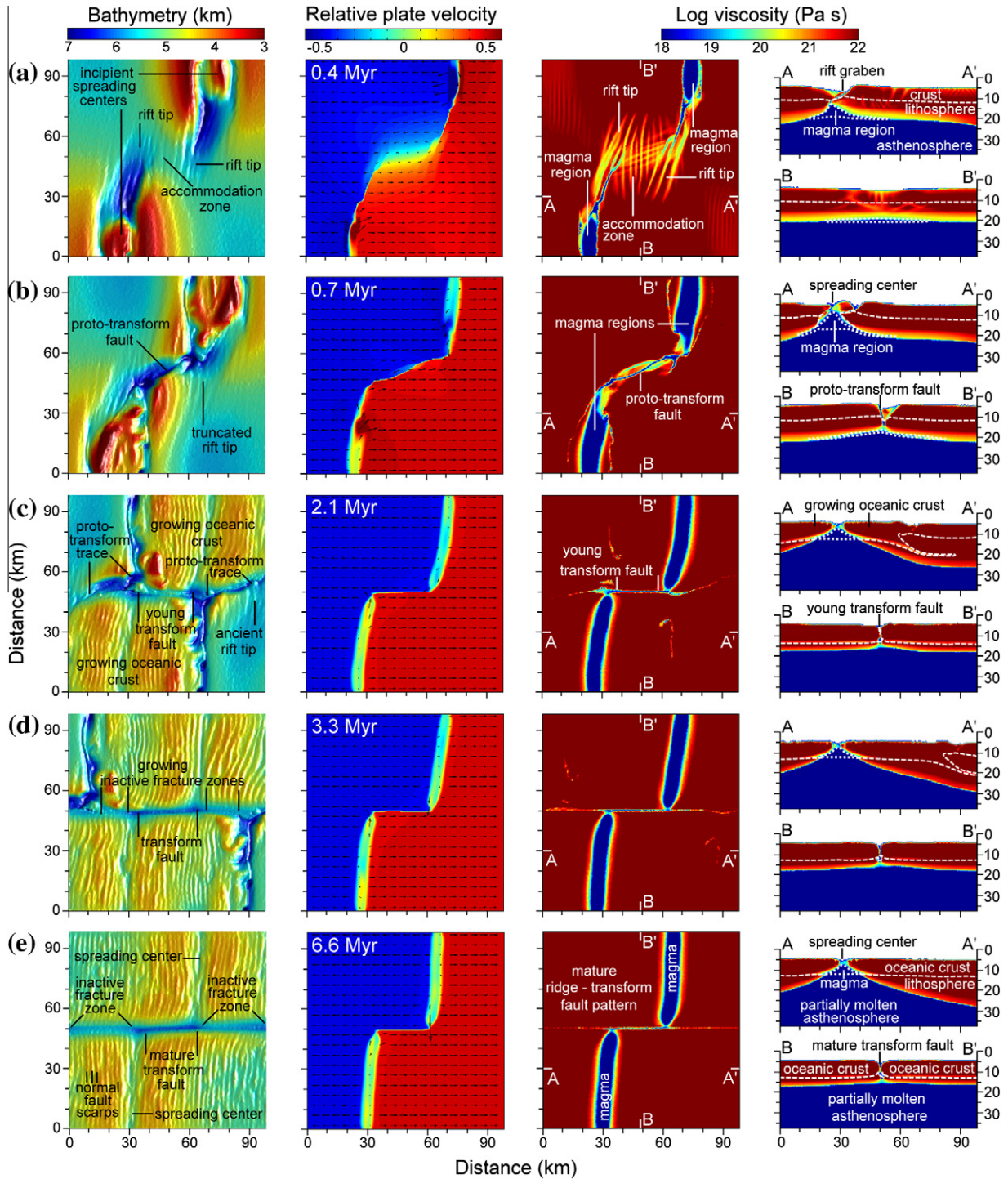


Fig. 3. Development of the orthogonal ridge – transform fault pattern after the onset of spreading (model “dart” in Table 1). Sea level for bathymetry maps (left column) corresponds to the top of the model. Horizontal velocity in the middle column is normalized to the spreading rate. Horizontal cross-sections for velocity and viscosity fields are taken at the level of 10 km from the top of the model. Strips on the surface of new oceanic crust correspond to normal fault scarps.

fault pattern. At the initial stages of the reference model development (Fig. 3a), two offset rift grabens form at the model margins atop the imposed thermal perturbations and start to propagate nearly orthogonal to the spreading direction. At around 0.4 Myr two magma regions form in the innermost part of the grabens as the result of decompression melting of rising asthenospheric mantle (Fig. 3a). Two elongated oceanic spreading centers nucleate at the surface and new oceanic crust starts growing by crystallization of melts along the walls of the magma regions (Fig. 3a). Spreading centers propagate toward each other and start to interact by forming an intermediate 20–30 km wide accommodation zone (Bosworth, 1986) that is oriented at $\sim 20^\circ$ to the spreading direction (Fig. 3b). The accommodation zone becomes narrower with time and at 0.5–0.7 Myr shrinks to a vertical proto-transform fault striking $\sim 20^\circ$ to the spreading direction (Fig. 3b). A 5–10 km wide and 0.5–1.5 km deep, elongated depression forms above this fault (Fig. 3b).

The orientation of the proto-transform fault ($\sim 20^\circ$ to the spreading direction) and the spreading centers ($\sim 75^\circ$ to the spreading direction) are different from the typical orthogonal pattern of mid-ocean ridges. The development of the proto-transform fault causes complete separation of two plates and truncates propagation of the spreading centers. Starting from 0.7 Myr the model development is dominated by magmatic accretion of new oceanic crust and gradual changes in the orientation of the proto-transform fault and the spreading centers toward an orthogonal pattern. Truncated tips of the spreading centers remain visible on the opposite plates (cf. two triangle-shaped regions of lowered seafloor topography in Fig. 3b and c). Inactive fracture zones start to form at around 2.5 Myr (Fig. 3c and d). The typical mature orthogonal pattern of two spreading centers offset by a transform fault bounded by two inactive fracture zones is established at around 3–4 Myr and remains stable through the rest of simulated model development (Fig. 3d and e).

3.2. Sensitivity of results to model parameters

According to the results of our experiments the resulting oceanic spreading pattern is strongly affected by the initial offset of the spreading centers and the magnitude of fracture healing rate, $\dot{\epsilon}_{\text{healing}}$ (Eq. (12)). Three different characteristic spreading modes were obtained by varying these two parameters (Fig. 4, Table 1): (1) ridge-transform patterns (Figs. 3, 5 and 6), (2) single ridges (Figs. 7 and 8) and (3) spreading centers with an intermediate plate (Fig. 9). Orthogonal and inclined ridge-transform patterns (see respectively pink and orange colors in Fig. 4) are stable at low healing rate of $\leq 10^{-13} \text{ s}^{-1}$ and intermediate offsets of 40–60 km. Single straight and curved ridges (see yellow color in Fig. 4) form both at low initial offsets (≤ 40 km) and at high fracture healing rates ($\geq 3 \times 10^{-13} \text{ s}^{-1}$). Spreading centers with an intermediate plate (this mode includes overlapping spreading centers with growing rotating microplate and parallel ridges with growing non-rotating middle plate, see blue color in Fig. 4) appear in models with large initial offsets (≥ 60 km). Indeed, gradual transitions between different spreading modes are observed during a single model development: transient ridge-transform pattern can evolve into a single ridge (Figs. 7 and 8), overlapping spreading centers with a rotating microplate can evolve into a ridge-transform pattern (Fig. 5). Transition between rotating and non-rotating regimes of intermediate plate development is also identified in some models (e.g., model “dasv” in Table 1 and Fig. 9). Also, it can be noticed that at relatively high fracture healing rate of $3 \times 10^{-12} \text{ s}^{-1}$ the orientation of the offset spreading centers deviates from being perpendicular to the spreading direction (see inclined ridge-transform patterns in Fig. 6f, i and j). On the other hand, zero fracture healing rate favors development of transient rotating microplates that later be-

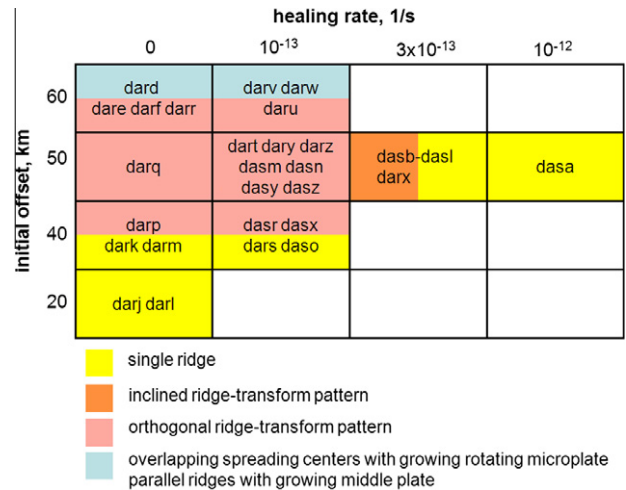


Fig. 4. Area diagram showing dependence of long-term oceanic spreading patterns on initial ridge offset and fracture healing rate $\dot{\epsilon}_{\text{healing}}$. Parameters for conducted numerical experiments listed in different cells are given in Table 1.

come accreted to one of the plates (models “dard”–“darr” in Table 1).

Other model parameters have less significant influence. Increasing the initial thermal thickness of the lithosphere to 29 km plays the same role as increasing the initial offset of the spreading centers: overlapping spreading centers with a growing rotating microplate are obtained in respective experiments (model “dasg” in Table 1). The initial thermal thickness of the plate also affects the nucleation time of the transform faults. This time becomes longer in models with thicker plates since more time is needed for initial plate rifting and subsequent nucleation of the oceanic spreading centers. Similarly to results of previous simplified oceanic spreading models (Gerya, 2010a), increasing the initial rock strength C_0 to 20 MPa produces coarser plate topography (Fig. 6g), stabilizes large-offset normal faults along the ridges (detachment faults), and results in larger degree of asymmetric plate accretion (model “dasy” in Table 1). On the other hand, variations in the imposed upper limit for plate viscosity (10^{22} – 10^{24} Pa s, Table 1) seem to have only a minor influence on the model development (cf. models “darx”, “dasb”, “dasc” in Table 1 and Fig. 6f, i and j) and does not significantly affect the resulting oceanic spreading pattern. The same observations apply to explored (rather subtle) variations in the following model parameters

- (1) the change in rheology of partially molten asthenosphere from constant viscosity of 10^{18} Pa s to dry olivine flow law (cf. models “dasj” and “dasl” in Table 1),
- (2) the moderate increase in the viscosity of the magma region to 10^{19} Pa s (cf. models “dask” and “dasd” in Table 1),
- (3) the variations of crustal thickness at constant thermal thickness of the lithosphere (cf. models “dasd” and “dasr” in Table 1),
- (4) the increase in the Nusselt number for the hydrothermal circulation from 2 to 4 (cf. models “dash” and “dasi” in Table 1),
- (5) the moderate acceleration of spreading rate from 3.8 to 5.7 cm/yr (cf. models “dash” and “dasd” in Table 1).

Indeed, larger variations in the spreading rate and in the Nusselt number (i.e. in the effective thermal conductivity of the crust) should have strong influence on the resulting spreading pattern as suggested by previous numerical experiments for long-term oceanic spreading (Gerya, 2010a).

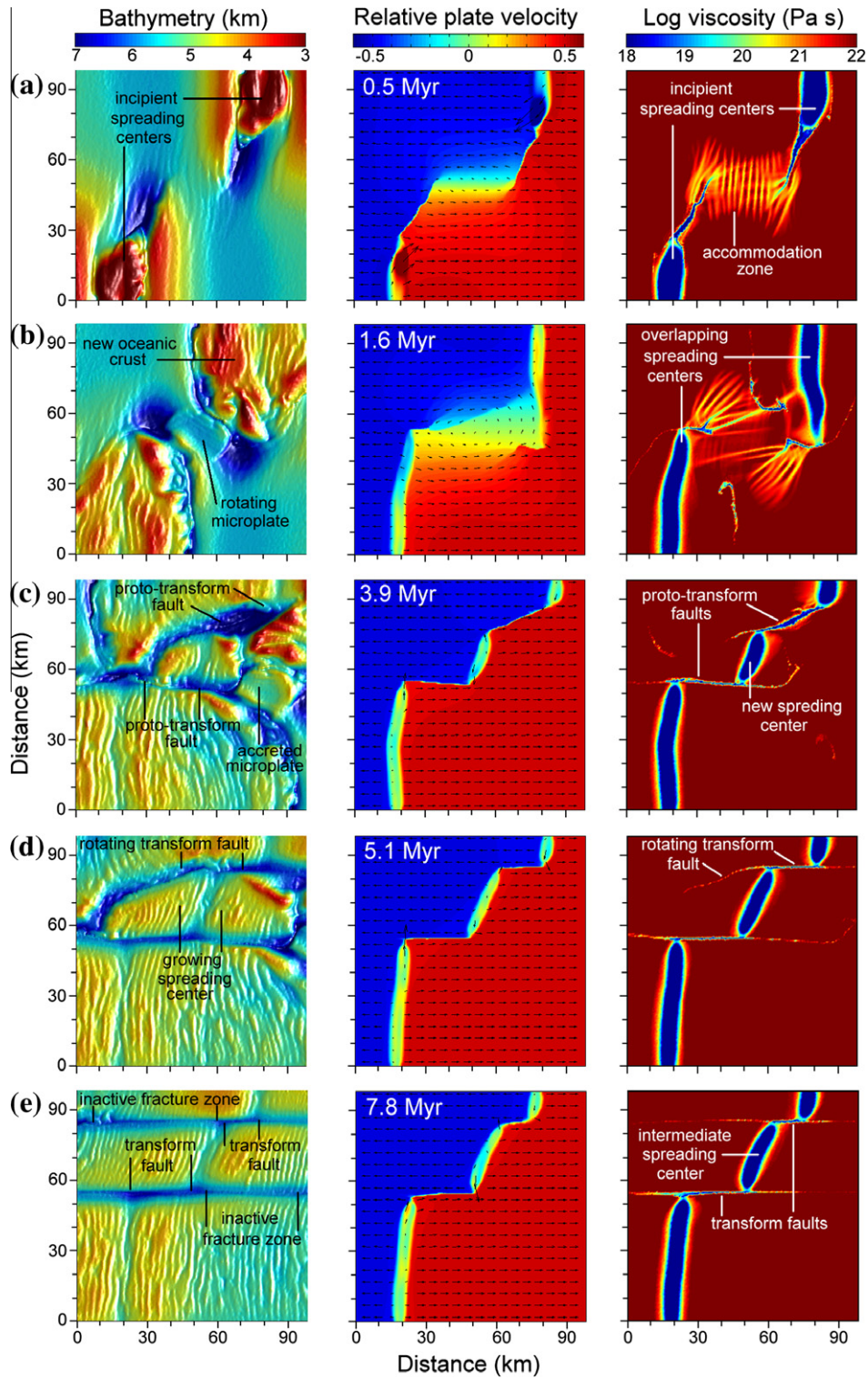


Fig. 5. Development of two transform faults with an intermediate spreading center following accretion of rotating microplate in the model with maximal initial ridge offset (60 km, model “daru” in Table 1).

4. Discussion

4.1. Comparison to previous models

Plate rifting patterns observed at the initial stages of model development in our experiments (Figs. 3 and 4a and b) are consistent with previous models and represent two out of five fundamen-

tal modes of plate fragmentation identified on the basis of numerical experiments by Hieronymus (2004). In particular, oblique linkage structures forming between offset spreading centers (Fig. 3a and b) were found in 3D numerical continental and oceanic rifting models (Choi et al., 2008; Allken et al., 2011, 2012), as well as in many analogue models with extending brittle lithosphere (Dau-teuil et al., 2002; Marques et al., 2007; Tentler and Accella, 2010).

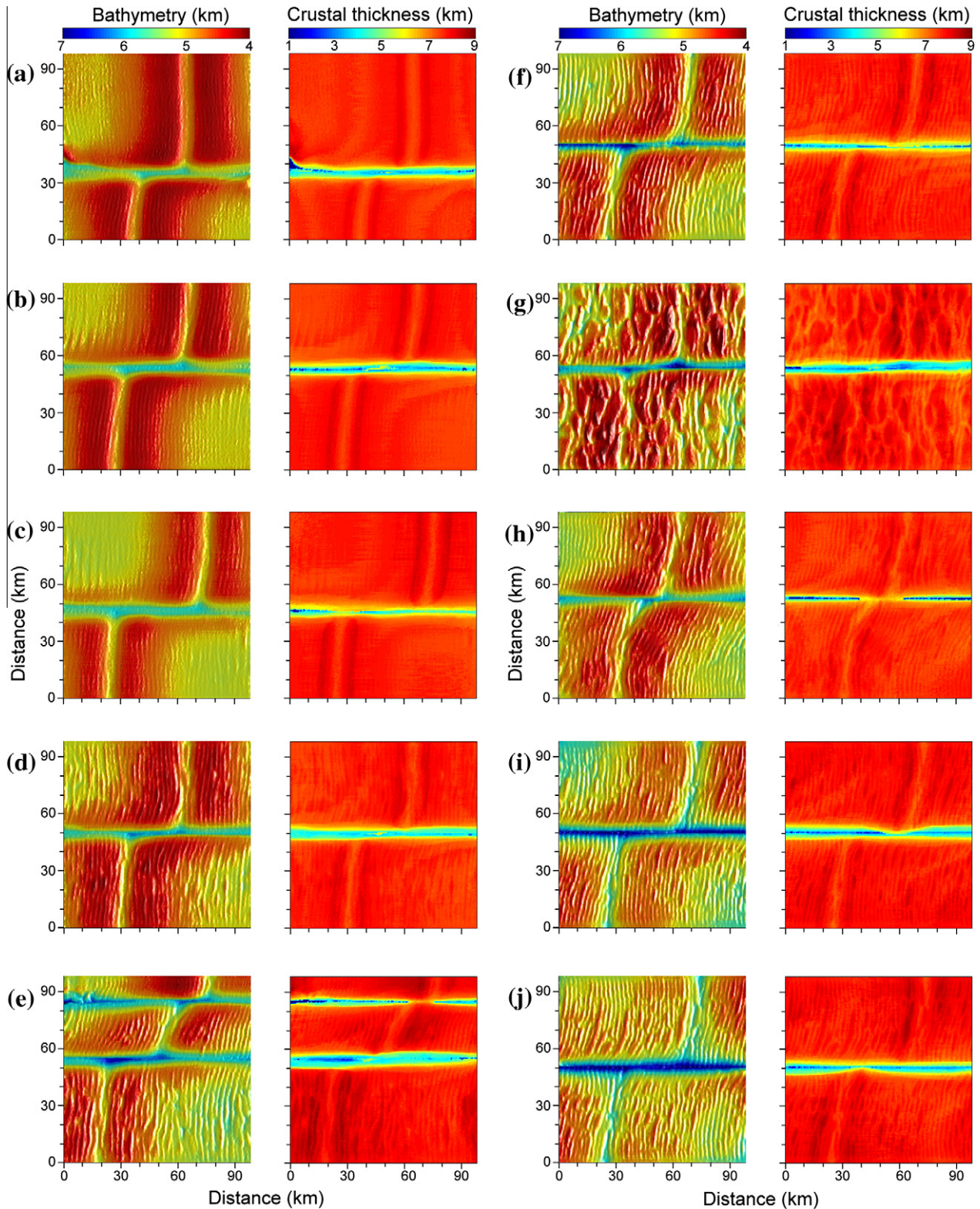


Fig. 6. Representative geometries and crustal thickness for mature orthogonal (a–e,g) and inclined (f, h–j) ridge-transform spreading patterns. Model parameters are given in Table 1: a = model “darp”, 7.9 Myr; b = model “darq”, 7.9 Myr; c = model “darr”, 8.0 Myr; d = model “dart”, 8.1 Myr; e = model “daru”, 7.8 Myr; f = model “darx”, 8.2 Myr; g = model “dary”, 6.5 Myr; h = model “darz”, 7.0 Myr; i = model “dasb”, 6.6 Myr; j = model “dasc”, 5.6 Myr.

Similarly, overlapping spreading centers (Fig. 4a and b) are also obtained in both analogue and numerical models of rifting (Choi et al., 2008; Tentler and Acocella, 2010; Allken et al., 2011). Indeed, in contrast to previous numerical and analogue models of rifting, our numerical experiments allowed for the long-term plate accre-

tion and studied development of mature ridge-transform spreading patterns from various initial rifting patterns. It should also be mentioned that both orthogonal ridge-transform spreading patterns and rotating tectonic microplates found in our models were previously obtained in freezing wax experiments (Oldenburg and Brune,

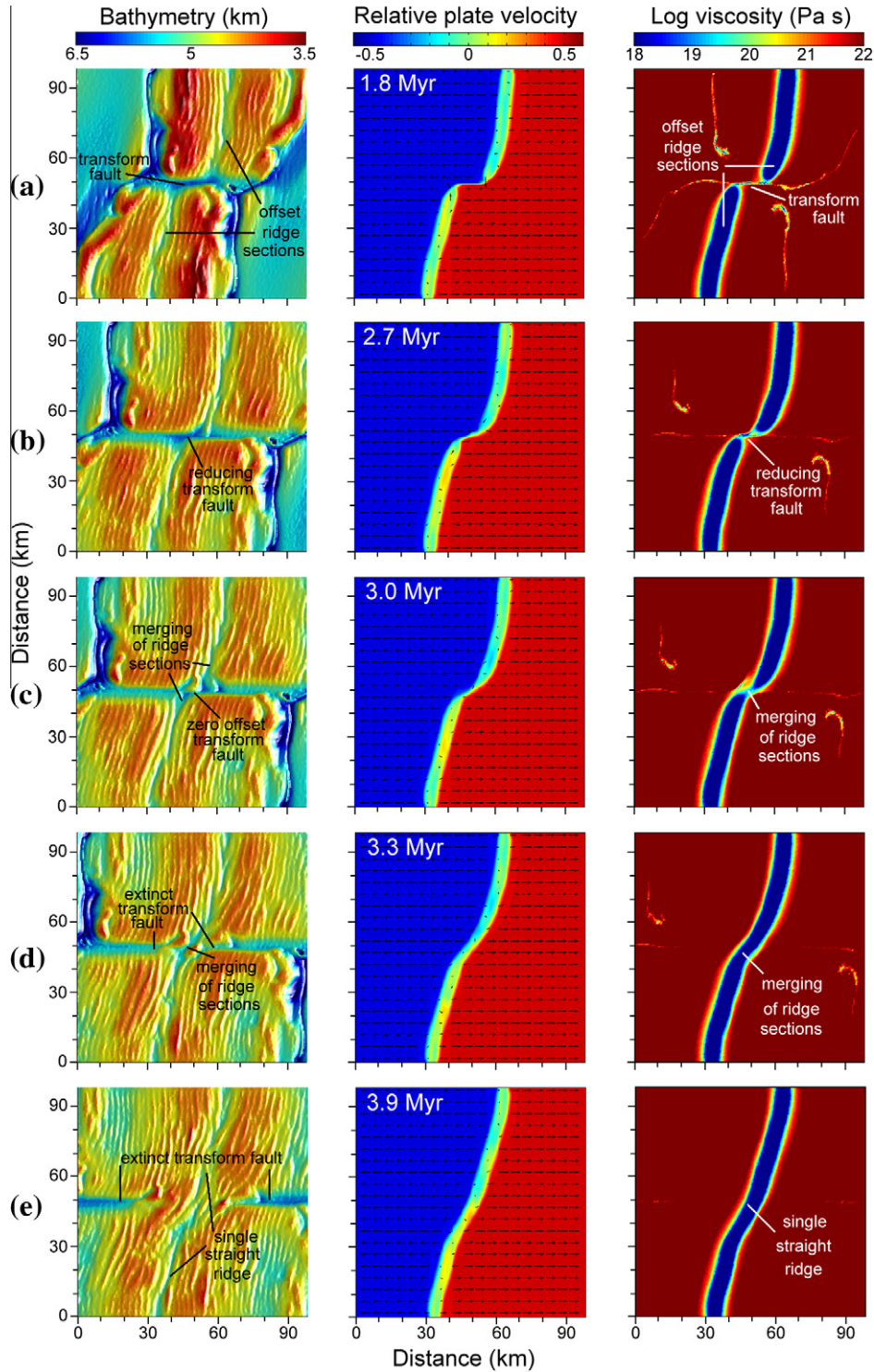


Fig. 7. Development of zero offset transform fault (zero offset fracture zone) and merging of initially offset ridge sections followed by stability of a single straight ridge (model “dars” in Table 1). Initial stages of model development correspond to transient stability of ridge-transform spreading pattern.

1972; O’Byrne et al., 1975; Katz et al., 2005), although these analogue models often produced open spreading centers with liquid wax coming to the surface, which is dissimilar to nature.

Compared to previous, simpler 3D models of oceanic spreading (Gerya, 2010a) that neglected pressure-dependent strength of confined brittle fractures, temperature-dependent viscosity of rocks and oceanic crust accretion, the present models show more symmetrical plate growth, relatively stable length of offset along trans-

form faults through time and a persistent development of inactive fracture zones (Fig. 3d and e). Test experiments show that the use of the temperature-dependent power-law rheology and the pressure-dependent brittle strength for confined fractures (Eq. (9)) are the main reasons for more symmetrical spreading patterns and systematic development of the inactive fracture zones observed in the present models. On the other hand, both previous and present spreading models demonstrate similar plate topogra-

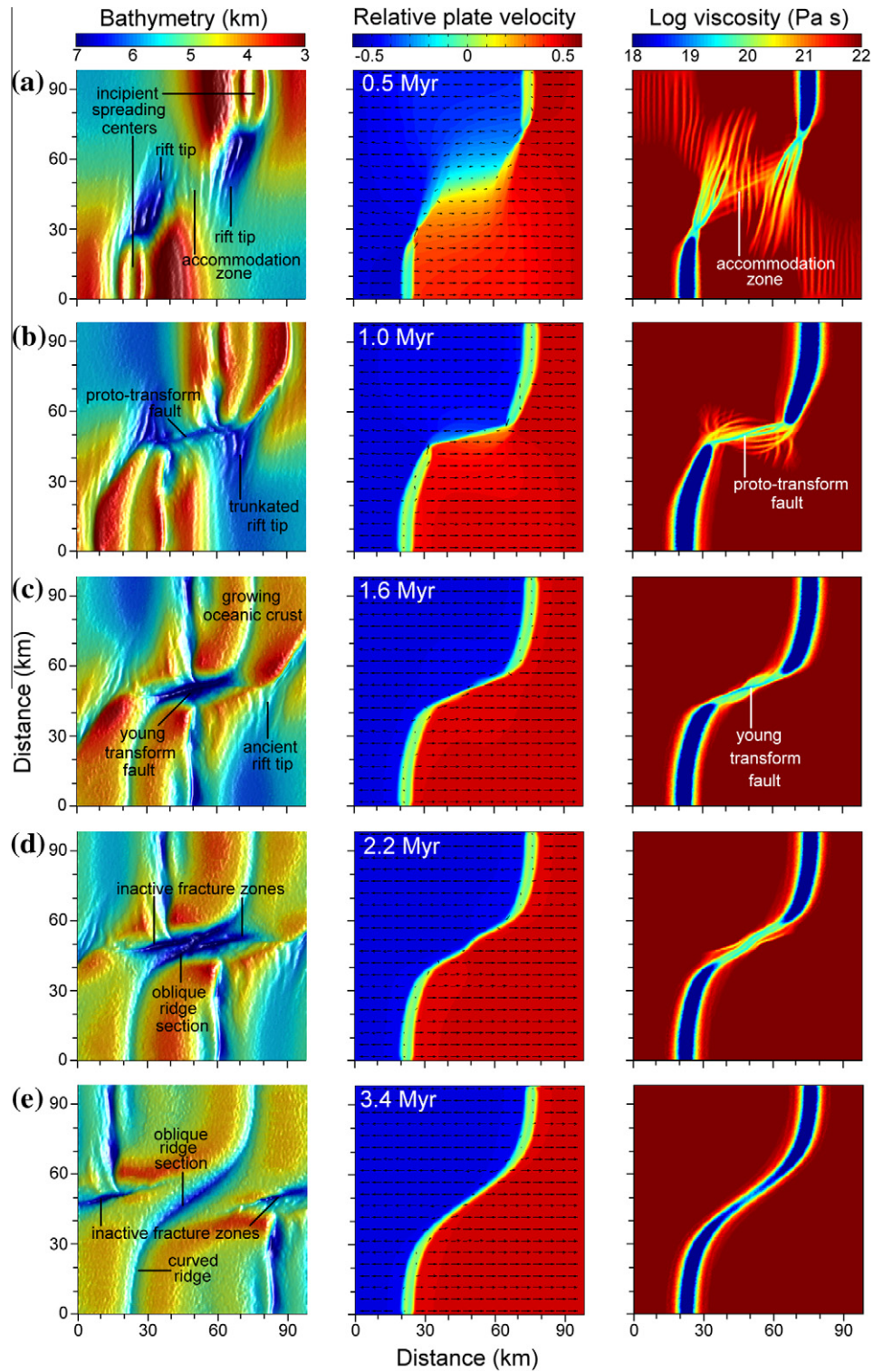


Fig. 8. Development of single curved ridge with an intermediate oblique section following short-term transient stability of young ridge-transform spreading pattern in the model with maximal fracture healing rate ($\dot{\epsilon}_{\text{healing}} = 10^{-12} \text{ s}^{-1}$, model “dasa” in Table 1).

phy patterns with a pronounced surface depression above the active transform faults (Fig. 6). Also, asymmetric plate accretion (mainly dependent on the initial strength of rocks C_0 , which defines magnitude of pressure-independent fracture weakening C_0-C_1 in Eq. (10)) is a persistent feature in the present models as well. This asymmetry often causes a reduction of offsets between spreading centers and leads to formation of zero offset transforms

(zero offset fracture zones, Fig. 7, Table 1). Formation of zero offset fracture zone causes merging of previously offset spreading centers into a single ridge, thus leading to the complete disappearance of the parent transform fault (Fig. 7). Similar close relations between the slight asymmetry in plate accretion and the appearance of zero offset transforms in nature was previously proposed by Stoddard and Stein (1988) on the basis of a simple mathematical model.

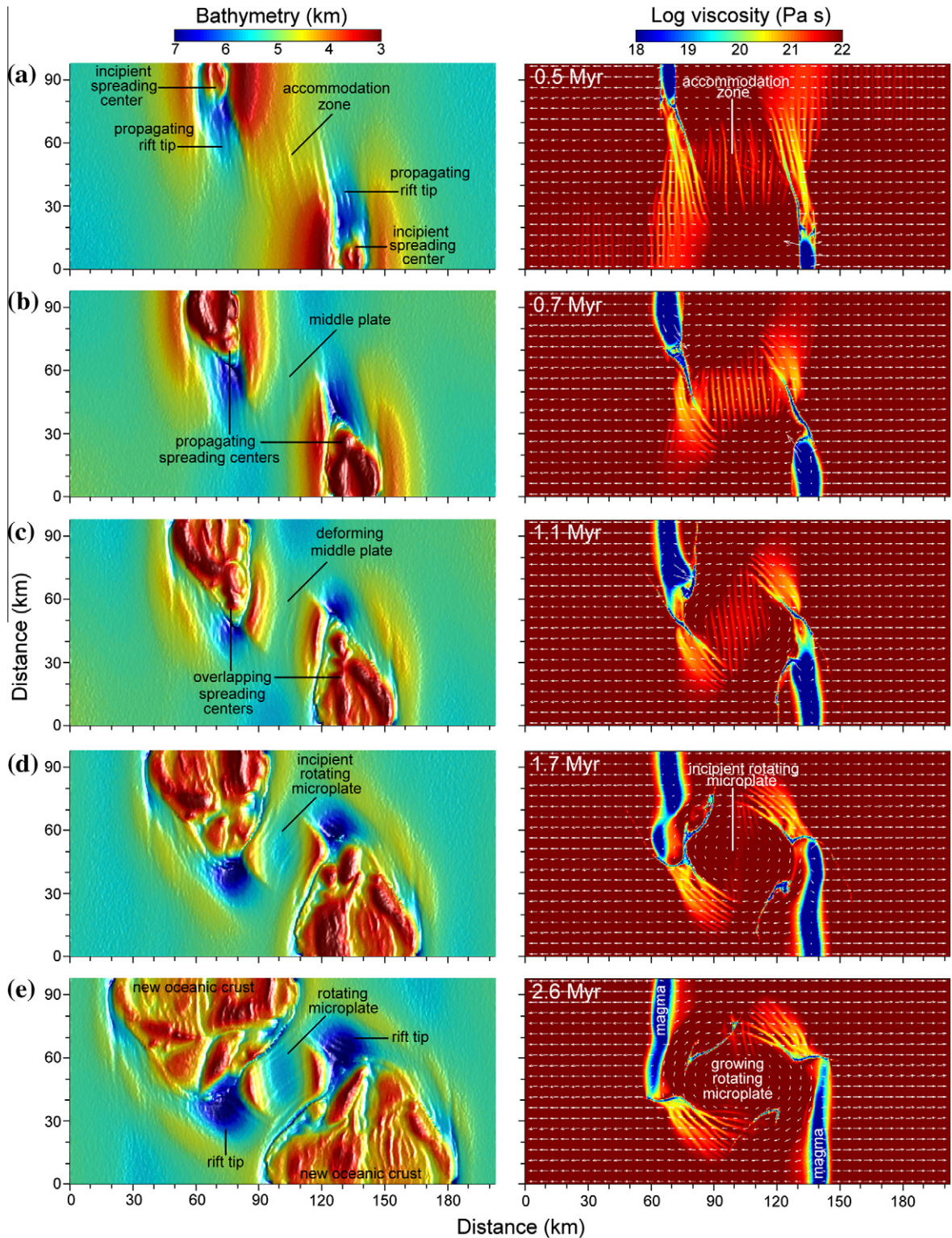


Fig. 9. Development of overlapping spreading centers with growing rotating microplate in the model with maximal initial ridge offset (60 km, model “dasv” in Table 1).

4.2. Evolution of transform fault orientation

Numerical experiments systematically show that transform faults often initiate at an angle to the spreading direction but then their orientation gradually changes toward the spreading-parallel. What is the reason of this behavior? Fig. 10 helps to understand the changes in the orientation of the transform fault with time. After establishment of the initial proto-transform fault connecting two

offset spreading centers, the spreading centers continue extending slowly toward the fault (Fig. 10(a–f)). This is because deformation within the proto-transform fault striking at an angle to the spreading direction is not purely strike-slip, but transtensional. The extensional component causes opening of the fault and accretion of the new oceanic crust at two ridge-fault intersections (Fig. 10(a–f)). Due to the sustaining weakness of the fault, the connection between the propagating tips of the spreading centers is

continuously re-established and thus causes rotation of the fault orientation toward the spreading-parallel direction. Two possible simple geometrical models of this process are discussed below.

According to the first geometrical model (Fig. 11a), the offset spreading centers always extend toward the displacing original rigid walls of the opening proto-transform fault established during the initial plate breakup. In this case, propagation rate (v_p) of the spreading centers toward each other remains constant with time and is given by simple geometric relation

$$v_p = v_s \times \text{tg}(\alpha_0), \quad (14)$$

where v_s is full spreading rate and α_0 is the initial deviation angle of the proto-transform fault from the spreading direction. Assuming that the frontal parts of the spreading centers will remain connected with an active transform fault, the orientation of this fault will change with time (t) as following

$$\text{tg} = \text{tg}(\alpha_0)[1 - v_s(t - t_0)/L], \quad (15)$$

where time t_0 corresponds to the moment of formation of initial proto-transform fault and L is the offset between spreading centers measured along the spreading-parallel direction (Fig. 11a), which remains constant through time. According to Eq. (15) the orientation of the proto-transform fault should rotate toward the spreading-parallel direction and will become spreading-parallel at the moment of time $t = t_0 + L/v_s$. Further rotation of the transform fault

will lead to a transpressional fault orientation, which precludes the offset segments sliding and is therefore unstable (e.g., Oldenburg and Brune, 1972). Spreading-parallel orientation ($\alpha = 0$) is thus the only thermomechanically consistent steady state orientation for the fault.

According to the second geometrical model (Fig. 11b), rigid walls of the active transform fault are reestablished together with changes of its orientation due to the fracture healing. In this case, propagation rate (v_p) of spreading centers toward each other depends on current fault orientation α (and not on the initial orientation of the proto-transform fault α_0 as in the first model), thus we have

$$v_p = v_s \times \text{tg}(\alpha). \quad (16)$$

The deviation angle of the fault in this case will change exponentially with time according to

$$\text{tg}\alpha = \text{tg}(\alpha_0) \times \exp[-v_s(t - t_0)/L]. \quad (17)$$

From Eq. (17) the orientation of the transform fault should asymptotically approach the spreading-parallel direction (i.e., $\alpha = 0$), which is again the only thermomechanically consistent steady state orientation.

Fig. 11c shows the comparison of results of numerical experiments (Fig. 10) with predictions of two geometrical models. As follows from this figure, the first geometrical model provides better fit for the results of numerical experiments, whereas the second model systematically underestimates changes in the transform fault orientation with time. Consequently, in numerical experiments transform fault rotation seems to be mainly regulated by the initial orientation of the parent proto-transform fault. It is important to mention that according to both tested geometrical models, propagation of spreading centers is limited by the rigid walls of the transform fault. This assumption is in apparent contrast with standard crack/rift propagation models proposed for the oceanic lithosphere (e.g., Pollard and Aydin, 1984), according to which propagating spreading centers can overlap and become bent toward each other. Indeed, the standard models assume an initially non-damaged plate without a weak transform connecting two propagating spreading centers. Consequently, similar type of behavior is observed in our models at the initial stages of development when the proto-transform fault is not yet formed (Fig. 3a, Fig. 9): rift tips of propagating spreading centers partly overlap and bend toward each other. In contrast, after the formation of the proto-transform fault, the rift propagation is truncated (Fig. 3b) and extensional deformation localizes inside this weak transensional fault, rather than inside its rheologically stronger walls.

The orientation change of the transform fault reduces the extensional component and enhances the strike-slip component of deformation within the fault. The spreading-parallel orientation of the transform fault is thus established as a steady state orientation allowing for pure strike-slip motion that stops the fault opening and thus the propagation of the spreading centers toward each other. The sustaining weakness of the fault (Oldenburg and Brune, 1972; Behn et al., 2002) and more importantly the ongoing accretion of new crust to the offset plate segments (Fig. 10a) are two pre-requisites for establishing this peculiar orientation. This orientation is thus mainly defined by geometrical requirements (180° rotational symmetry for open space occupation, Eqs. (14) and (15), Fig. 11a) for simultaneous accretion and displacement of new plate material within two offset spreading centers connected by a sustaining weak fault. It can be, therefore, notably different from the physics of plate fragmentation (Hieronymus, 2004; Choi et al., 2008; Allken et al., 2011). This points toward a fundamental difference between the geometry of the initial rifting pattern (a

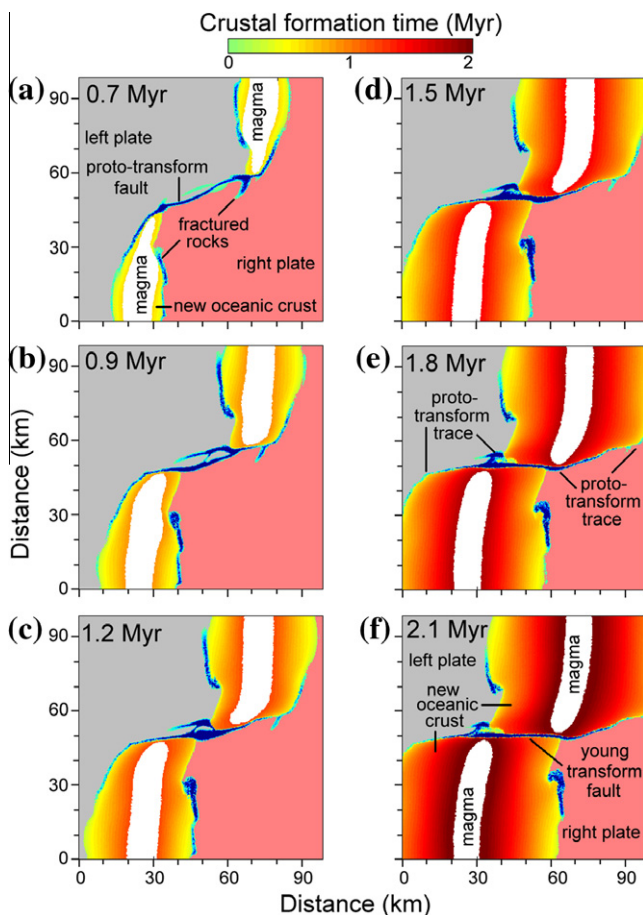


Fig. 10. Changes in the proto-transform fault orientation with time for the reference model shown in Fig. 3. Color code: white = magma region, blue = fractured rocks, yellow to red = new oceanic crust (formation time corresponds to the moment of crystallization from the melt), pink and gray = initial plate material for the right and left plate, respectively. Horizontal cross-sections are taken at the level of 10 km from the top of the model. (For interpretation of the references to color in this figure legend, the reader is referred to the web version of this article.)

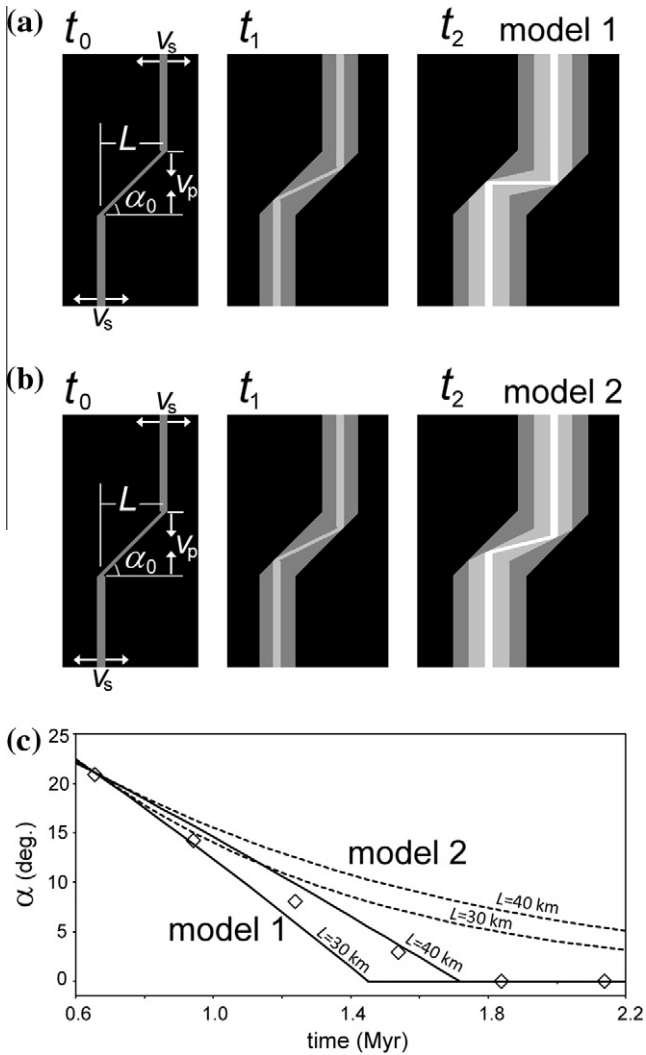


Fig. 11. Geometrical concepts of transform fault re-orientation. (a and b) conceptual schemes of crustal growth associated with the transform fault reorientation (different colors show crust of different age) for two geometrical models discussed in the text. (c) comparison of analytical (lines, Eqns. (15) and (17) are respectively used for model 1 and model 2 with $v_s = 3.8$ cm/yr, $t_0 = 0.66$ Myr, $\alpha_0 = 21^\circ$ and $L = 30\text{--}40$ km, where variations in L account for gradual decrease in the spreading-parallel offset between propagating tips of the spreading centers measured in Fig. 10) and numerical (symbols, data are taken from Fig. 10) models.

plate fragmentation pattern) and that of a mature ridge-transform spreading pattern (a plate growth pattern). This difference is to some degree analogous to the difference between a fragment of a thin broken ice plate (ice fragmentation structure) and a snowflake (ice growth structure). Further thermomechanical reasons for the stability of weak extension-parallel transforms could be related to minimization of energy dissipation (e.g., Bercovici, 1995).

The documented rotation of the transform fault orientation is a robust model feature, which systematically appears at different numerical resolutions (Fig. 3a–c and Fig. 12). Performed resolution tests also confirm that the numerical grid spacing used in the majority of experiments is optimal and further increase in the resolution does not significantly change transform fault nucleation and rotation dynamics (Fig. 3a–c and Fig. 12e and f). On the other hand, a notable decrease in the resolution causes earlier (by 0.1–0.2 Myr) localization of the proto-transform fault, however subsequent crustal growth and fault rotation dynamics remain similar to the reference model (Figs. 3 and 12a–c).

4.3. Comparison with natural data

Mature transform faults and inactive fracture zones formed in the experiments (Figs. 3e, 5e, 6) are comparable to nature. They are expressed by narrow depressions in the ocean floor topography (Gregg et al., 2007; Taylor et al., 2009; DeMets et al., 2010) and show thinned (by 1–5 km) oceanic crust characteristic for these structures at slow to intermediate spreading rates (Kuo and Forsyth, 1988; Lin and Phipps Morgan, 1992; Tolstoy et al., 1993). Near the ridge-transform intersection, the pattern of seafloor faulting is often slightly asymmetric (Fig. 3e): normal fault scarps extending from the segment center into inside-corner crust curve in the offset direction, while fault scarps extending into outside-corner crust typically remain parallel to the ridge (Phipps Morgan and Parmentier, 1984). Zero offset transforms (Fig. 7c) are also documented in nature (Schouten and White, 1980; Stoddard and Stein, 1988). One possible example of large rotating tectonic microplates found in our experiments (Fig. 9e) is the Easter microplate in which rift propagation has resulted in the formation of a rigid plate between the propagating and dying ridges (Engeln and Stein, 1984; Cogné et al., 1995). On the other hand, overlapping spreading centers (Fig. 5b, Fig. 9c) occurring in nature (e.g., Macdonald et al., 1984; Sempere and Macdonald, 1986) are characterized by much smaller offsets (up to 15 km) and are found in fast spreading ridges, which are not explored in this study.

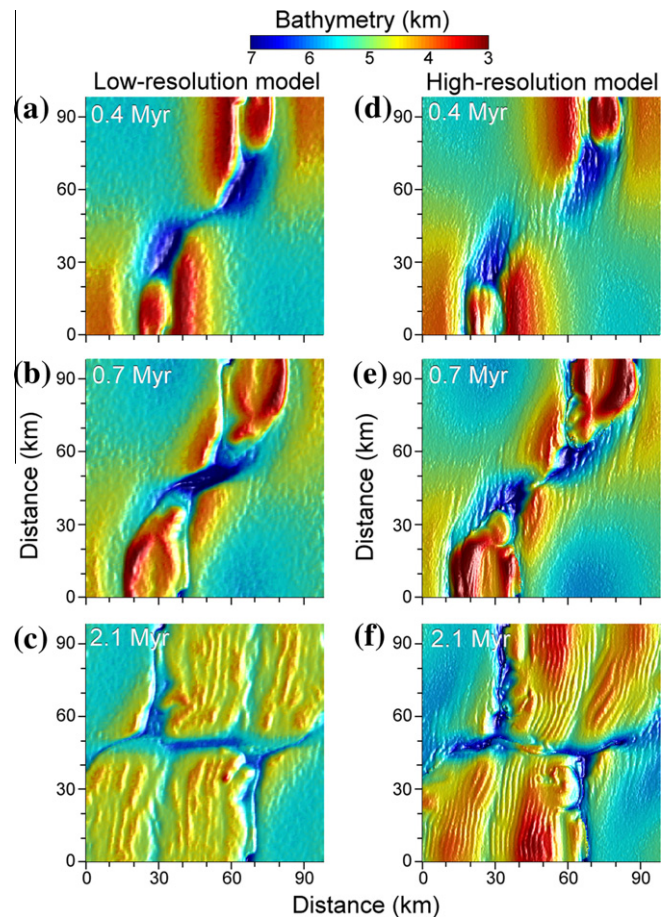


Fig. 12. Results of numerical resolution test for the reference model ($197 \times 197 \times 101$ nodes, 34 million markers) shown in Fig. 3a–c. (a–c) Low-resolution model ($133 \times 133 \times 69$ nodes, 11 million markers). (d–f) High-resolution model ($293 \times 293 \times 149$ nodes, 105 million markers). Strain weakening and healing in the experiments is linearly scaled to the grid step compared to the reference model: $\gamma_0 = 0.7$, $\dot{\epsilon}_{\text{healing}} = 0.7 \times 10^{-13}$ for low-resolution model, $\gamma_0 = 1.5$, $\dot{\epsilon}_{\text{healing}} = 1.5 \times 10^{-13}$ for high-resolution model.

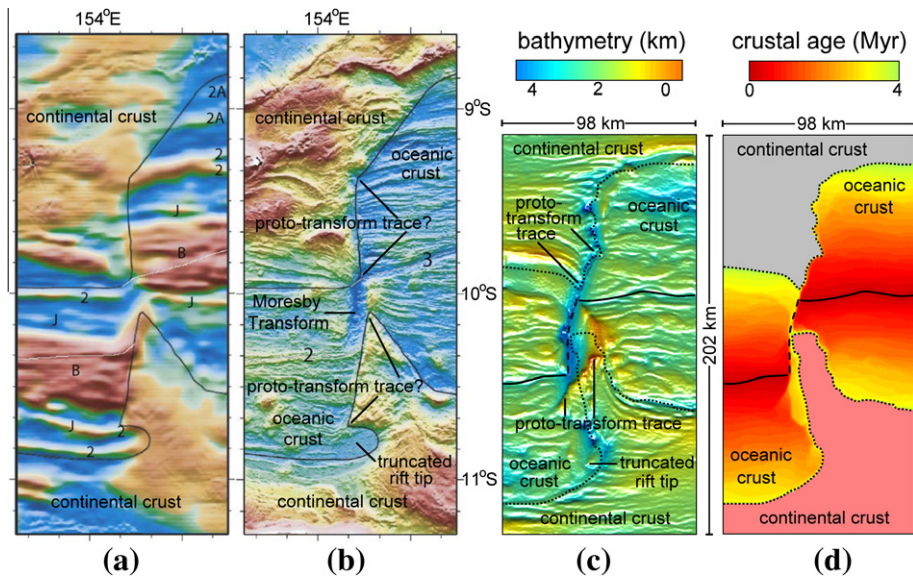


Fig. 13. Comparison of natural data for the incipient spreading in the Woodlark basin (a,b) (Taylor et al., 2009) with the results of numerical experiments (c and d, model “dask” in Table 1). (a) Magnetization of the Moresby Transform (that may correspond to a rotating proto-transform fault) and its conjugate margins (with lineations labeled for Brunhes (B), Jaramillo (J), anomaly 2 and 2A). (b) Sunlit bathymetry (with spreading segments 2 and 3 labeled). (c and d) modeled bathymetry and oceanic crustal age distribution on the surface, respectively. Black solid line in (a) and (b) shows continent-ocean boundary. Solid, dashed and dotted lines in (c) and (d) show spreading segments, proto-transform fault and continent-ocean boundary, respectively.

Incipient oceanic spreading patterns obtained in numerical models correlate well with available data on natural examples (Fig. 13). In particular, (proto-) transform faults in the Woodlark Basin terminate in the oceanic crust (Fig. 13a and b) and formed while linking two offset spreading segments on the timescale of around 0.5–2 Myr (Taylor et al., 2009). Our numerical models reproduce well characteristic “rounded” contours of two spreading centers as well as the presence of an island of the continental crust observed in the Woodlark basin (Fig. 13b and Fig. 13d). When a proto-transform fault nucleates in the continental domain (Figs. 3 and 10), its walls control the propagation of offset oceanic spreading centers toward each other (Fig. 10). Proto-transform fault will thus leave traces on two opposite curved boundaries between the oceanic and continental domains (Figs. 3c, 10e). Proto-transform fault traces and truncated tips of overlapping spreading centers present in models (Figs. 3b,c and 13c) are also documented in nature (Fig. 13b). It should be mentioned, however, that the models presented here are still highly simplified and assume synchronous opening of two ridge sections, whereas in the Woodlark basin, the eastern section of the ridge starts to form before the western section does (Taylor et al., 2009, see anomalies 2A present east of the Moresby transform only in Fig. 13a). Nevertheless, the first order dynamics of the Moresby (proto-)transform should be properly captured in the model since this fault started to develop at a stage when both rift sections were simultaneously active (Taylor et al., 2009).

Numerical models shown here predict that only a limited range of initial ridge offsets (40–60 km) can produce stable ridge-transform spreading patterns. This is in contrast with much broader variations of transform offsets (0–900 km) in nature (e.g., Sandwell, 1986; Stoddard and Stein, 1988). One possible explanation for this discrepancy is that transform offset can change with time (e.g., Fig. 7) due to asymmetric plate accretion (e.g., Stoddard and Stein, 1988; Gerya, 2010a). Indeed, random variations in spreading asymmetry may provide an explanation for development of very small to zero offsets (Stoddard and Stein, 1988). However, such random variations have difficulty generating significant increases in transform length, so very long transforms may be manifestations of dynamic processes (Stoddard and Stein, 1988). These processes

can be related to (i) the presence of large lithospheric-scale heterogeneities inside breaking plates (absent in our simplified experiments), which could be inherited by long proto-transform faults and (ii) the sustaining asymmetry of plate accretion at relatively slow spreading rates that may cause systematic increase of transform offsets during initial (slow) stages of oceanic spreading (Gerya, 2010a).

5. Conclusions

According to the results of our experiments, oceanic spreading pattern depends strongly on the initial offset of spreading centers and the magnitude of fracture healing rate. Three different characteristic long-term spreading modes are obtained: (1) ridge-transform patterns, (2) single ridges and (3) spreading centers with an intermediate plate.

Orthogonal ridge-transform oceanic spreading patterns in nature should typically form few million years after the continental/oceanic plate breakup and should be generally different from the initial plate rifting pattern.

Proto-transform faults can nucleate in the beginning of oceanic spreading by the dynamic interaction of growing offset spreading centers. The orientation of these structures should change with time, with a tendency toward the spreading-parallel direction.

The orthogonal ridge-transform system is a long-term plate growth pattern, which is governed by geometrical requirements (180° rotational symmetry for open space occupation) for simultaneous accretion and displacement of new plate material within two offset spreading centers, connected by a sustaining, rheologically weak transform fault. According to these requirements, the characteristic spreading-parallel orientation of oceanic transform faults is the only thermomechanically consistent steady state orientation.

Acknowledgments

J.-P. Burg and D.A. May are thanked for discussions and comments. This work was supported by ETH Research Grants ETH-

0807-2, ETH-0807-3, ETH-0609-2, SNF Research Grants 200020-126832, 200020-129487, SNF ProDoc program 4-D-Adamello, TopoEurope Program and Crystal2Plate program. Constructive reviews by D. Bercovici, J.-P. Brune and an anonymous reviewer are appreciated.

References

- Allken, V., Huismans, R.S., Thieulot, C., 2011. Three-dimensional numerical modeling of upper crustal extensional systems. *J. Geophys. Res.* 116, B10409.
- Allken, V., Huismans, R.S., Thieulot, C., 2012. Factors controlling the mode of rift interaction in brittle-ductile coupled systems: a 3D numerical study. *Geochem. Geophys. Geosyst.* 13, Q05010.
- Behn, M.D., Lin, J., 2000. Segmentation in gravity and magnetic anomalies along the US east coast passive margin; implications for incipient structure of the oceanic lithosphere. *J. Geophys. Res.* 105, 25769–25790.
- Behn, M.D., Lin, J., Zuber, M.T., 2002. Evidence for weak transform faults. *Geophys. Res. Lett.* 29. <http://dx.doi.org/10.1029/2002GL015612>.
- Bercovici, D., 1995. On the purpose of toroidal motion in a convecting mantle. *Geophys. Res. Lett.* 22, 3107–3110.
- Bercovici, D., Ricard, Y., 2012. Mechanisms for the generation of plate tectonics by two-phase grain-damage and pinning. *Phys. Earth Planet. Inter.* 202–203, 27–55.
- Bosworth, W., 1986. Comment on detachment faulting and the evolution of passive continental margins. *Geology* 14, 890–891.
- Buck, W.R., Lavier, L.L., Poliakov, A.N.B., 2005. Modes of faulting at mid-ocean ridges. *Nature* 434, 719–723.
- Buiter, S.J.H., Babeyko, A.Yu., Ellis, S., Gerya, T.V., Kaus, B.J.P., Kellner, A., Schreurs, G., Yamada, Y., 2006. The numerical sandbox: Comparison of model results for a shortening and an extension experiment. In: Buiter, S.J.H., Schreurs, G. (Eds.), *Analogue and Numerical Modelling of Crustal-Scale Processes*. Geological Society London Special Publications 253, pp. 29–64.
- Choi, E., Lavier, L., Gurnis, M., 2008. Thermomechanics of mid-ocean ridge segmentation. *Phys. Earth Planet. Inter.* 171, 374–386.
- Clauser, C., Huenges, E., 1995. Thermal conductivity of rocks and minerals. In: Ahrens, T.J. (Ed.), *Rock Physics and Phase Relations AGU Reference Shelf 3*. American Geophysical Union, Washington DC, pp. 105–126.
- Cochran, J.R., Martinez, F., 1988. Evidence from the northern Red Sea on the transition from continental to oceanic rifting. *Tectonophysics* 153, 25–53.
- Cogné, J.P., Francheteau, J., Courtillot, V., 1995. Pit093 scientific team large rotation of the Easter microplate as evidenced by oriented paleomagnetic samples from the ocean floor. *Earth Planet. Sci. Lett.* 136, 213–222.
- Connolly, J.A.D., Schmidt, M.W., Solferino, G., Bagdassarov, N., 2009. Permeability of asthenospheric mantle and melt extraction rates at mid-ocean ridges. *Nature* 462, 209–212.
- Cramer, F., Schmeling, H., Golabek, G.J., Duret, T., Orendt, R., Buiter, S.J.H., May, D.A., Kaus, B.J.P., Gerya, T.V., Tackley, P.J., 2012. A comparison of numerical surface topography calculations in geodynamic modelling: an evaluation of the 'sticky air' method. *Geophys. J. Int.* 189, 38–54.
- Dauteuil, O., Brun, J.-P., 1993. Oblique rifting in a slow-spreading ridge. *Nature* 361, 145–148.
- Dauteuil, O., Brun, J.-P., 1996. Deformation partitioning in a undergoing oblique extension: Mohs Ridge, Norwegian Sea. *Tectonics* 15, 870–884.
- Dauteuil, O., Bourgeois, O., Mauduit, T., 2002. Lithosphere strength controls oceanic transform zone structure: insights from analogue models. *Geophys. J. Int.* 150, 706–714.
- DeMets, C., Gordon, R.G., Argus, D.F., 2010. Geologically current plate motions. *Geophys. J. Int.* 181, 1–80.
- Engeln, J.F., Stein, S., 1984. Tectonics of the Easter plate. *Earth Planet. Sci. Lett.* 68, 259–270.
- Escartin, J., Hirth, G., Evans, B., 2001. Strength of slightly serpentinized peridotites: implications for the tectonics of oceanic lithosphere. *Geology* 29, 1023–1026.
- Gerya, T., 2010a. Dynamical instability produces transform faults at mid-ocean ridges. *Science* 329, 1047–1050.
- Gerya, T.V., 2010b. Introduction to Numerical Geodynamic Modelling. Cambridge University Press, Cambridge, UK.
- Gerya, T., 2012. Origin and models of oceanic transform faults. *Tectonophysics* 522–523, 34–56.
- Gerya, T.V., Yuen, D.A., 2007. Robust characteristic method for modeling multiphase visco-elasto-plastic thermo-mechanical problems. *Phys. Earth Planet. Inter.* 163, 83–105.
- Gregg, P.M., Behn, M.D., Lin, J., Grove, T.L., 2009. Melt generation, crystallization, and extraction beneath segmented oceanic transform faults. *J. Geophys. Res.* 114, B11102.
- Gregg, P.M., Lin, J., Behn, M.D., Montesi, L.G.J., 2007. Spreading rate dependence of gravity anomalies along oceanic transform faults. *Nature* 448, 183–187.
- Hieronymus, C.F., 2004. Control on seafloor spreading geometries by stress- and strain-induced lithospheric weakening. *Earth Planet. Sci. Lett.* 222, 177–189.
- Hilairet, N., Reynard, B., Wang, Y., Daniel, I., Merkel, S., Nishiyama, N., Petitgirard, S., 2007. High-pressure creep of serpentine, interseismic deformation, and initiation of subduction. *Science* 318, 1910–1913.
- Huismans, R.S., Beaumont, C., 2002. Asymmetric lithospheric extension: the role of frictional plastic strain softening inferred from numerical experiments. *Geology* 30, 211–214.
- Jaeger, J.C., 1963. Extension failures in rocks subject to fluid pressure. *J. Geophys. Res.* 68, 6066.
- Jarrige, J.J., Ott d'Estevou, P., Burollet, P.F., Montemar, C., Richert, J.P., Thiriet, J.P., 1990. The multistage tectonic evolution of the Gulf of Suez and northern Red Sea continental rift from field observations. *Tectonics* 9, 441–465.
- Katz, R.F., 2010. Porosity-driven convection and asymmetry beneath mid-ocean ridges. *Geochem. Geophys. Geosyst.* 11, Q0AC07.
- Katz, R.F., Spiegelman, M., Langmuir, C.H., 2003. A new parameterization of hydrous mantle melting. *Geochem. Geophys. Geosyst.* 4, 1073.
- Katz, R.F., Ragnarsson, R., Bodenschatz, E., 2005. Tectonic microplates in a wax model of sea-floor spreading. *New J. Phys.* 7. <http://dx.doi.org/10.1088/1367-2630/7/1/037>.
- Kuo, B.Y., Forsyth, D.W., 1988. Gravity anomalies of the ridge transform intersection system in the South Atlantic between 31 and 34.5°S: upwelling centers and variations in crustal thickness. *Mar. Geophys. Res.* 10, 205–232.
- Lavier, L.L., Buck, W.R., Poliakov, A.N.B., 2000. Factors controlling normal fault offset in an ideal brittle layer. *J. Geophys. Res.* 105, 23431–23442.
- Lin, J., Phipps Morgan, J., 1992. The spreading rate dependence of three-dimensional mid-ocean ridge gravity structure. *Geophys. Res. Lett.* 19, 13–16.
- Lister, G.S., Etheridge, M.A., Symonds, P.A., 1986. Detachment faulting and the evolution of passive continental margins. *Geology* 14, 246–250.
- Lyakhovskiy, V., Ben-Zion, Y., 2008. Scaling relations of earthquakes and aseismic deformation in a damage rheology model. *Geophys. J. Int.* 172, 651–662.
- Macdonald, K.C., Sempere, J.-C., Fox, P.J., 1984. The East Pacific Rise from the Siqueiros to the Orozco fracture zone: a long-strike continuity of the neovolcanic zone and the structure and evolution of overlapping spreading centers. *J. Geophys. Res.* 89, 6049–6069.
- Marques, F.O., Cobbold, P.R., Lourenço, N., 2007. Physical models of rifting and transform faulting, due to ridge push in a wedge-shaped oceanic lithosphere. *Tectonophysics* 443, 37–52.
- McClay, K., Khalil, S., 1998. Extensional hard linkages, eastern Gulf of Suez. *Egypt. Geol.* 6, 563–566.
- Montesi, L.G.J., Behn, M.D., Hebert, L.B., Lin, J., Barry, J.L., 2011. Controls on melt migration and extraction at the ultraslow Southwest Indian Ridge 10 degrees-16 degrees E. *J. Geophys. Res.* 116, B10102.
- Murrell, S.A.F., 1964. The theory of propagation of elliptical Griffith cracks under various conditions of plane strain or plain stress. Parts 2, 3. *Br. J. Appl. Phys.* 15, 1123.
- Nikolaeva, K., Gerya, T.V., Connolly, J.A.D., 2008. Numerical modelling of crustal growth in intraoceanic volcanic arcs. *Phys. Earth Planet. Inter.* 171, 336–356.
- O'Byrne, J.W., Cohen, R., Gilliland, W.N., 1975. Experimental origin of transform faults and straight spreading-center segments. *GSA Bull.* 86, 793–796.
- Oldenburg, D.W., Brune, J.N., 1972. Ridge transform fault spreading pattern in freezing wax. *Science* 178, 301–304.
- Olive, J.-A., Behn, M.D., Tucholke, B.E., 2010. The structure of oceanic core complexes controlled by the depth distribution of magma emplacement. *Nat. Geosci.* 3, 491–495.
- Hess, P.C., 1989. *Origin of Igneous Rocks*. Harvard University Press, London, UK.
- Phipps Morgan, J., Parmentier, E., 1984. Lithospheric stress near a ridge transform intersection. *Geophys. Res. Lett.* 11, 113–116.
- Pollard, D.D., Aydin, A., 1984. Propagation and linkage of oceanic ridge segments. *J. Geophys. Res.* 89, 10017–10028.
- Ragnarsson, R., Ford, J.L., Santangelo, C.D., Bodenschatz, E., 1996. Rifts in spreading wax layers. *Phys. Rev. Lett.* 76, 3456–3459.
- Ranalli, G., 1995. *Rheology of the Earth*. Chapman & Hall, London, UK.
- Rosendahl, B.R., 1987. Architecture of continental rifts with special reference to East Africa. *Ann. Rev. Earth Planet. Sci. Lett.* 15, 445–503.
- Rozhko, A.Y., Podladchikov, Y.Y., Renard, F., 2007. Failure patterns caused by localized rise in pore-fluid overpressure and effective strength of rocks. *Geophys. Res. Lett.* 34, L22304.
- Sandwell, D., 1986. Thermal stress and the spacings of transform faults. *J. Geophys. Res.* 91, 6405–6417.
- Sempere, J.C., Macdonald, K.C., 1986. Overlapping spreading centers: Implications from crack growth simulation by the displacement discontinuity method. *Tectonics* 5, 151–163.
- Schmeling, H., Babeyko, A.Y., Enns, A., Faccenna, C., Funicello, F., Gerya, T., Golabek, G.J., Grigull, S., Kaus, B.J.P., Morra, G., Schmalholz, S.M., van Hunen, J., 2008. Benchmark comparison of spontaneous subduction models – towards a free surface. *Phys. Earth Planet. Inter.* 171, 198–223.
- Schouten, H., White, R.S., 1980. Zero-offset fracture zones. *Geology* 8, 175–179.
- Stoddard, P.R., Stein, S., 1988. A kinematic model of ridge-transform geometry evolution. *Mar. Geophys. Res.* 10, 181–190.
- Taylor, B., Goodliffe, A., Martinez, F., Hey, R.N., 1995. Continental rifting and initial seafloor spreading in the Woodlark Basin. *Nature* 374, 534–537.
- Taylor, B., Goodliffe, A., Martinez, F., 2009. Initiation of transform faults at rifted continental margins. *C.R. Geosci.* 341, 428–438.
- Theissen-Krah, S., Iyer, K., Rüpke, L.H., Phipps Morgan, J., 2011. Coupled mechanical and hydrothermal modeling of crustal accretion at intermediate to fast spreading ridges. *Earth Planet. Sci. Lett.* 311, 275–286.

- Tentler, T., Acocella, V., 2010. How does the initial configuration of oceanic ridge segments affect their interaction? Insights from analogue models. *J. Geophys. Res.* 115, B01401.
- Tolstoy, M., Harding, A., Orcutt, J., 1993. Crustal thickness on the Mid-Atlantic Ridge: bulls-eye gravity anomalies and focused accretion. *Science* 262, 726–729.
- Turcotte, D.L., Schubert, G., 2002. *Geodynamics*. Cambridge University Press, Cambridge.
- Wanless, V.D., Shaw, A.M., 2012. Lower crustal crystallization and melt evolution at mid-ocean ridges. *Nat. Geosci.* 5, 651–655.
- Watts, A.B., Stewart, J., 1998. Gravity anomalies and segmentation of the continental margin offshore West Africa. *Earth Planet. Sci. Lett.* 156, 239–252.
- Wilson, J.T., 1965. A new class of faults and their bearing on continental drift. *Nature* 207, 343–347.